Single pass computation of first seismic wave travel time in three dimensional heterogeneous media with general anisotropy

François Desquilbet, Jian Cao, Paul Cupillard, Ludovic Métivier, Jean-Marie Mirebeau

▶ **To cite this version:**

François Desquilbet, Jian Cao, Paul Cupillard, Ludovic Métivier, Jean-Marie Mirebeau. Single pass computation of first seismic wave travel time in three dimensional heterogeneous media with general anisotropy. 2021. hal-03244537v1

HAL Id: hal-03244537

https://hal.science/hal-03244537v1

Preprint submitted on 1 Jun 2021 (v1), last revised 6 Oct 2021 (v3)

HAL is a multi-disciplinary open access archive for the deposit and dissemination of scientific research documents, whether they are published or not. The documents may come from teaching and research institutions in France or abroad, or from public or private research centers.

L'archive ouverte pluridisciplinaire **HAL**, est destinée au dépôt et à la diffusion de documents scientifiques de niveau recherche, publiés ou non, émanant des établissements d'enseignement et de recherche français ou étrangers, des laboratoires publics ou privés.

Single pass computation of first seismic wave travel time in three dimensional heterogeneous media with general anisotropy

François Desquilbet[*], Jian Cao[†], Paul Cupillard [‡], Ludovic Métivier[§], Jean-Marie Mirebeau[¶]

June 1, 2021

Abstract

We present a numerical method for computing the first arrival time of seismic waves in media defined by a general Hooke tensor, in contrast with previous methods which are limited to a specific subclass such as the "tilted transversally isotropic" (TTI) model or "tilted orthorhombic" (TOR) model [WYF15, LBBMV19]. Our method proceeds in a single pass over the discretized domain, similar to the Fast Marching method, whereas existing methods for these types of anisotropies require multiple iterations, similar to the Fast Sweeping method. We introduce a new source factorization model, allowing us to achieve third order accuracy in smooth test cases. We also validate our solver by comparing it with the solution of the elastic wave equation on a 3D medium with general anisotropy.

Keywords eikonal equation · travel-time computation · fast marching schemes · anisotropy · 3D

1 Introduction

The eikonal equation characterizes the first arrival time of a front, propagating inside a domain at a speed dictated by a given metric. In geophysics, an eikonal equation can be obtained as the high-frequency approximation of a wave equation, with the underlying metric defined by the properties of the geological medium.

Computing the solution of the wave equation in three dimensional complex media can be expensive. Indeed, the scale of the discretization grid needs to be substantially smaller than the oscillation wavelength, while the time step is itself bounded due to the Courant-Friedrichs-Levy stability condition. In contrast, the eikonal equation is a static (no time dependency) partial differential equation, whose solution is non-oscillatory. For this reason, efficient schemes for the eikonal equation have been developed along the years, with several applications in mind: earthquake hypocenter relocation through backpropagation of the data recorded at the surface by seismic stations [MvN92], asymptotic approximation of Green's functions for Kirchhoff migration to build high resolution images in seismic exploration [Bey87, Ble87, LOP$^+$03], or tomographic

[*]Univ. Grenoble Alpes, LJK, F-38000, Grenoble, France
[†]Univ. Grenoble Alpes, ISTerre, F-38000, Grenoble, France
[‡]Univ. de Lorraine, Georessources, F-54000, Nancy, France
[§]Univ. Grenoble Alpes, CNRS, LJK, ISTerre, F-38000, Grenoble, France
[¶]Univ. Paris-Saclay, CNRS, Centre Borelli, 91190, Gif-sur-Yvette, France

inversions to determine seismic wave velocities from global and regional scale [Nol08] to exploration and near surface scale targets [BL98, TNCC09] .

However, the metrics from geophysics are often anisotropic, which has been a technical challenge for the numerical solvers designed for the eikonal equation. Anisotropy can occur from the shape of minerals, with for example the olivine that can be found in the uppermost mantle under oceans [Hes64] and can lead to a preferred direction up to 25% faster than other directions. Besides, thin sedimentary layers of isotropic materials can also be treated as an anisotropic medium in order to smooth strong heterogeneities. It usually leads to a homogenized medium with a faster horizontal speed compared with vertical speed, which is called "vertical transverse isotropy" (VTI) in terms of symmetry in the Hooke tensor. Some shifts can also occur with tectonic movements, leading to the "tilted transverse isotropy" (TTI). More complex anisotropies have been considered in the case of fractures, leading to "tilted orthorhombic" (TOR) symmetry or a fully general Hooke tensor.

One option to compute first arrival traveltimes is the well-established ray-tracing method [Cer05]. However, several drawbacks have been identified: one ray does not necessarily correspond to the first arrival time, the computation cost increases strongly when many travel paths to many points are needed, and calculations can be difficult in shadow zones which can occur even in a smooth medium. These issues no longer occur when solving the eikonal equation with finite-difference schemes. Note that, conversely, computing second or later arrival times with an eikonal solver is a non-trivial problem [RS04], which is not further discussed in this paper.

The first finite-difference scheme for the eikonal equation has been developed by Vidale [Vid88], in the isotropic case only and with first-order accuracy, and it has later been extended to anisotropy [Lec93]. This solver works by induction on the boundary of a square expanding from the source point, but it has no guarantee of success in the case of strong heterogeneity or anisotropy: causality cannot be guaranteed if ever a ray goes back into the expanding square. This method lacks the robustness and guarantees of an approach based on strong theoretical foundations.

In [OS91], the isotropic eikonal equation is solved by treating it as a dynamic (time-dependent) Hamilton-Jacobi equation, with an "essentially non-oscillatory" (ENO) scheme. This approach has been extended to VTI anisotropy and high-order accuracy in [DS97], with the "down & out" (DNO) strategy. A post-treatment (PS) is added in [KC99], with second-order accuracy, resulting in the ENO-DNO-PS scheme, which was extended to TTI anisotropy in [Kim99]. However, the method is computationally expensive. Some other algorithms have been considered to solve the dynamic eikonal equation, but algorithms for the static (time-independent) eikonal equation have been found to be more efficient [LBBMV17].

More efficient algorithms have then been developed thanks to the level-set framework [Set96], and the numerical solution of the static eikonal equation as considered in this paper. These numerical methods can be divided into two classes: *iterative* methods and *single pass* methods, which respectively generalize the algorithms of Bellman-Ford and of Dijkstra for graph distance computation. The best known iterative method is presumably the Fast Sweeping Method (FSM). Originally introduced in the isotropic setting [Zha05], the FSM has been extended to 2D elliptic anisotropy [TCOZ03], 2D TTI symmetry [LCZ14], 3D TTI symmetry [PWZ17] with a third-order Lax-Friedrich fast sweeping scheme, 3D TOR symmetry [WYF15] treated as an iterative problem

on elliptic anisotropy, and more recently [LBBMV19] for the 3D TOR symmetry with high-order accuracy. Other iterative methods include the Adaptive Gauss-Siedel Iteration (AGSI) [BR06], or the Buffered Fast Marching (BFM) method [Cri09], which can both handle some amount of anisotropy. Recently, iterative methods have been proposed that take advantage of massively parallel computational architectures, graphics processing units in particular, in the isotropic setting [JW08], and for elliptic anisotropy [GHZ18].

On the other hand, the best single pass method is presumably the Fast Marching Method (FMM) [Tsi95, Set96], but the extension of the FMM to anisotropic geometries proved more difficult. Early works [KS98, SV01, AM12] involve wide stencil numerical schemes, leading to increased computation times and reduced accuracy, and therefore negating many of the advantages of the FMM, see the end of this introduction. More recently [bW20], an algorithm using the FMM has been developed for the 3D TTI anisotropy: it works by solving a fixed point problem on VTI elliptic anisotropy. While the authors illustrate numerically that the algorithm can converge when the target anisotropy is not too far from an elliptic VTI anisotropy, there is no formal proof of convergence of the fixed point iteration they implement.

In the past years, one of the authors has proposed extensions of the FMM to 2D anelliptic anisotropy [Mir14b], and 3D elliptic anisotropy [Mir14a, Mir19], as well as various types of degenerate anelliptic anisotropy related with curvature penalization [Mir18]. In these works, techniques from lattice geometry allow to keep the size of the discretization stencil under tight control, thus preventing any loss in computation time and accuracy, even for very strong anisotropies (with propagation speed $10\times$ faster in some directions than others). In this paper, we propose a numerical solver using the FMM to solve the eikonal equation with an anelliptic anisotropy defined by a general Hooke tensor. Such a general anisotropy is usually mildly pronounced in absolute terms (with propagation speed at most twice faster in some directions than others) but nevertheless it raises a number of specific computational challenges. The method we develop here can be implemented up to third order accuracy, as illustrated in the numerical experiments §4.

When discussing about the anisotropy of a metric, we make a distinction between two concepts: its "strength" and its "complexity". The strength of the anisotropy refers to the ratio between the highest and lowest achievable speed, depending on the orientation at a given position. The complexity of the anisotropy refers to the number of parameters needed to characterize the metric: for three-dimensional media, 1 parameter is needed for isotropic metrics, 6 parameters for Riemannian metrics (elliptic anisotropy), 8 parameters for TTI metrics, 12 parameters for orthorhombic metrics, and finally 21 parameters for metrics defined by a fully general Hooke tensor. For two-dimensional media, 1 parameter is needed for isotropic metrics, 3 for Riemanian metrics, 5 for TTI metrics and 6 for a fully general Hooke tensor. Our numerical scheme can handle the most complex metrics with all 21 parameters from the Hooke tensor. Such fully general Hooke tensors can arise from homogenization procedures, see [CC18] and §4.2. However, we still have a limitation on the strength of the anisotropy that we can handle: the fast marching method is applicable to our scheme as long as the strength of anisotropy is lower than a given bound, depending on the discretization stencils, see §2.3. (In the event where this condition fails, the correct solution to our scheme can nevertheless be computed using an iterative method such as fast sweeping, see Appendix D.) We checked that we could tackle the strength of anisotropy from most cases found in seismical media, see Table 1 and Figure 2.

Throughout this paper, $\mathbb{R}^d$ denotes the usual Euclidean space, where $d \in \{2, 3\}$ is the ambient

dimension. A closed, bounded and connected subset $\Omega \subset \mathbb{R}^d$ is fixed, representing the physical domain. It is equipped with a positive density field $\rho : \Omega \to \mathbb{R}$, as well as a field of Hooke 4th-order tensors $c(x) = (c_{ijkl}(x))$, where $i, j, k, l \in \{1, \cdots, d\}$, describing the elastic properties of the medium, with the usual symmetry assumptions (minor and major symmetries). For any point $x \in \Omega$ and any $p \in \mathbb{R}^d$, regarded as a co-vector, we define

$$m_x(p)_{ik} := \frac{1}{\rho(x)} \sum_{j,l} c_{ijkl}(x) p_j p_l, \qquad N_x^*(p) = \sqrt{\|m_x(p)\|}. \tag{1}$$

Thus $m_x(p)$ is a $d \times d$ symmetric matrix, and $N_x^*(p)$ is the square root of its spectral norm. Note the homogeneity relations $m_x(\lambda p) = \lambda^2 m_x(p)$ and $N_x^*(\lambda p) = |\lambda| N_x^*(p)$ for any $\lambda \in \mathbb{R}$. Unless stated otherwise, summation as in (1) over the indices i, j, k, or l is from 1 to d. We assume that the Hooke tensor $c(x)$ is strictly elliptic, ensuring that $m_x(p)$ is positive definite for all $p \neq 0$ and that N_x^* is a norm on $\mathbb{R}^d$, see Definition 3.1 and Remark 3.5 in §3.1.

In this paper, we present an efficient numerical method for computing the unique viscosity solution $u : \Omega \to \mathbb{R}$, see [BCD08], of the generalized eikonal equation

$$N_x^*(\nabla u(x)) = 1, \tag{2}$$

for all $x \in \mathrm{int}(\Omega) \setminus \{x_0\}$, where x_0 is a prescribed source point. This equation is complemented with the boundary condition $u(x_0) = 0$ at the source, and outflow boundary conditions on $\partial\Omega$. One can rewrite (2) under the following classical form [Sla03] which stems from the high frequency analysis of elastic waves:

$$\det\Big(\sum_{j,l} c_{ijkl}(x) \partial_j u(x) \partial_l u(x) - \rho(x)\delta_{ik}\Big) = 0, \tag{3}$$

where δ_{ik} denotes Kronecker's symbol. Equation (2) contains the additional information that only the fastest propagation speed is considered. Note that lower propagation speeds formally yield an eikonal equation similar to (2) but involving a non-convex Hamiltonian in general instead of (1, right). Therefore their viscosity solution does not correspond to a travel time of the P-SV modes in the elastic wave equation, but yields non-physical values corresponding to the convex envelope of the Hamiltonian.

We introduce a discretization of the PDE (2), which is solved in a single pass over the domain, using a variant of the FMM. As the algorithm progresses, the successive values $u(x_0) \leq u(x_1) \leq u(x_2) \leq \cdots$ of the numerical solution on Ω_h are computed and then frozen, one by one and in increasing order. The algorithm is *strictly causal*, in the sense that the numerical value $u(x_n)$ computed at a given point only depends on already frozen and strictly smaller values of the solution $u(x_m) < u(x_n)$, $m < n$. This property of the discretized system reflects the deterministic nature of the wave front motion: a present arrival time only depends on the earlier ones, and not on the future ones.

In comparison with iterative methods, such as fast sweeping [TCO04], adaptive Gauss-Seidel iterations [BR06], or buffer based methods [Cri09], the FMM used here has a number of appealing properties:

- Robustness. The FMM does not require setting any stopping criterion, and is deterministically guaranteed to terminate in a finite number of steps. In addition it is able to tackle general anisotropy associated with a general Hooke tensor $c_{ijkl}(x)$.

- Speed. The running time of the FMM is $\mathcal{O}(N \ln N)$, *independently of the problem instance*, in contrast with sweeping methods which require a variable number of sweeps depending on the medium complexity (dozens in a complex seismic medium, hundreds in some applications to medical image processing [Mir14a]). A variant of the FMM [Tsi95, RS07] achieves $\mathcal{O}(N)$ complexity, and some level of parallelism, but due to the large hidden constant in the complexity estimate it is rarely used.

- Accuracy. Simple enhancements to the FMM allow to formally achieve second and third order accuracy [Set99], which is confirmed in the numerical experiments §4. Such high order schemes are required to estimate the elastic wave amplitudes, or the curvature of the front, whose computation involves second-order spatial derivatives of the arrival times.

- Differentiability. The Jacobian matrix of the FMM has a sparse and upper triangular structure, allowing for efficient inversion by direct substitution [MD17].

- Extensibility. *Dynamic Fast Marching* methods modify the numerical scheme on-line, as the front propagation proceeds, depending on various properties of the minimal paths such as their curvature [LRr13]. In the context of seismic imaging, this flexibility could be used to take into account non-linear effects due to amplitude [VN18].

On the negative side, setting up the FMM for non-isotropic metrics requires substantial work, depending on the geometrical properties of the equation solved [KS98, SV01, AM12, Mir14b, Mir14a, Mir18, Mir19]. In the present state, our numerical method is bound by the following limitations:

- Parallelism. The FMM is intrinsically sequential, and thus cannot take advantage of parallel or massively parallel architectures such as [JW08, GHZ18].

- Stencil construction and size. The discretization stencils need to obey specific angular properties, depending on the nature and the strength of the anisotropy. Since the overwhelming majority of materials encountered in seismology feature rather mild anisotropy, in absolute terms, our generalized fast marching method can be usually instantiated with a compact stencil known as the cut-cube, see Figures 1 and 2. However, for crystals such as mica, which are some of the most anisotropic materials encountered in seismology, somewhat more extended stencils must be used, see Figure 1 (right), at the possible expense of speed and accuracy. In addition, extending our approach from Cartesian grids to unstructured grids would require substantial effort, in the spirit of [KS98, LFH11].

Outline: An overview of the proposed numerical scheme is presented in §2. Implementation details for the critical routines are detailed in §3. Numerical experiments presented in §4 illustrate the method accuracy and computational efficiency. Finally, we present a conclusion with future perspectives in §5.

2 The fast marching method

This section describes (a generalization of) the fast marching method [Tsi95], that is used in this paper to solve the generalized eikonal equation (2). The discussion in this section applies to general anelliptic metrics, see Definition 2.7, and the implementation details related with the specific algebraic form (3) of the equation encountered in seismic imaging are postponed to §3. The first two subsections §2.1 and §2.2 introduce classical mathematical tools, that are at the

foundation of our approach. The main contributions of this section lie in the angular distortion estimates of §2.3, and the choice of source factorization (20) in §2.4. A summary of the method is presented in §2.5.

The physical domain Ω is discretized on a Cartesian grid of scale $h > 0$,

$$\Omega_h := \Omega \cap h\mathbb{Z}^d, \tag{4}$$

and we assume for simplicity that the source $x_0 \in \Omega_h$.

2.1 Geometrical formulation of the eikonal equation.

The generalized eikonal equation (2) is written in terms of a norm N_x^*, at each point $x \in \Omega$, on the space of co-vectors[1]. Following [BCD08] we characterize its unique solution in geometrical terms, involving a norm N_x on vectors, and a distance map between points. For any $v \in \mathbb{R}^d$, regarded as a vector, define

$$N_x(v) := \max\{\langle p, v\rangle;\ p \in \mathbb{R}^d,\ N_x^*(p) \leq 1\}. \tag{5}$$

In the context of seismic imaging, the norm N_x has no closed form expression, but is defined by the above optimization problem in terms of the dual norm N_x^* which is itself the root of a third degree polynomial (1, right). Our numerical scheme depends on the efficient numerical computation of $N_x(v)$ and of its gradient, which is discussed in §3.

Denote by $\Gamma := \mathrm{Lip}([0,1], \overline{\Omega})$ the set of all paths within the domain closure, with locally Lipschitz regularity. The length of a path $\gamma \in \Gamma$, and the distance between two points $x, y \in \overline{\Omega}$, are defined as

$$\mathcal{L}(\gamma) := \int_0^1 N_{\gamma(t)}(\gamma'(t))\,\mathrm{d}t, \qquad d(x,y) := \min\{\mathcal{L}(\gamma);\ \gamma \in \Gamma, \gamma(0) = x, \gamma(1) = y\}.$$

The unique viscosity solution to the eikonal equation (2) is the distance from the source point [BCD08]

$$u(x) = d(x_0, x). \tag{6}$$

From this characterization, one can derive Bellman's optimality principle, stating that for any $x \in \Omega \setminus \{x_0\}$, and any neighborhood $\mathcal{V} \subset \Omega$ of x not containing the source point x_0, one has

$$u(x) = \min_{y \in \partial\mathcal{V}} u(y) + d(y, x). \tag{7}$$

2.2 Discretization of the eikonal equation

Following [KS98, SV01, BR06, Mir14a, Mir14b], our discretization of the eikonal equation (2) mimics and discretizes Bellman's optimality principle (7). For that purpose, we introduce for each $x \in \Omega_h$ a polygonal neighborhood $\mathcal{V}_h^x$ whose vertices lie on $h\mathbb{Z}^d$ (recall that $\Omega_h := \Omega \cap h\mathbb{Z}^d$), referred to as the stencil, along with a piecewise linear interpolation operator $\mathcal{I}_h^x$ on its facets. Given $u : \Omega_h \to \mathbb{R}$ we approximate the r.h.s. of (7) by interpolating the arrival times between the vertices of the stencil, and approximating the distance function with the local norm:

$$\Lambda_h u(x) = \min_{y \in \partial\mathcal{V}_h^x} \mathcal{I}_h^x\, u(y) + N_x(x - y). \tag{8}$$

[1] In this paper, the distinction between vectors and co-vectors is kept at an informal level, and we do not distinguish between the spaces $\mathbb{R}^d$ and $(\mathbb{R}^d)^*$

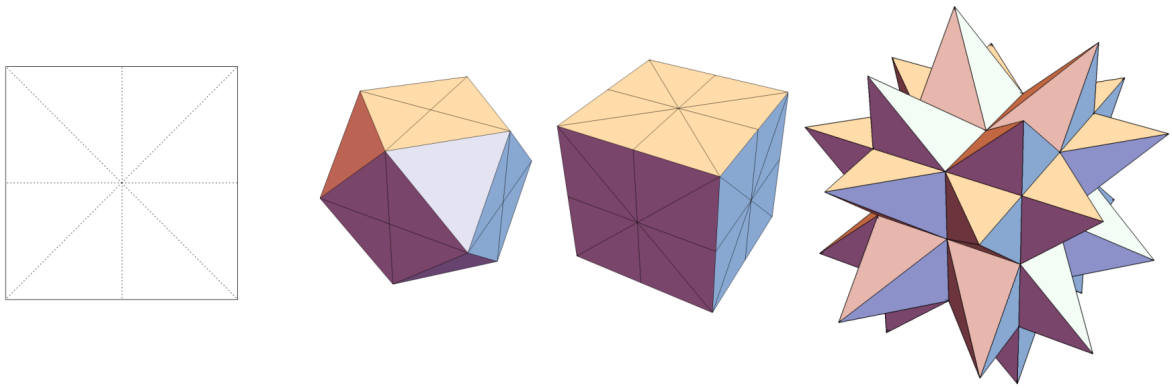

Figure 1: Stencils used, in dimension 2 (square) and 3 (cut-cube, cube and spiky-cube)

The function u is extended by $+\infty$ on $h\mathbb{Z}^d \setminus \Omega_h$ in (8), which naturally implements outflow boundary conditions on $\partial\Omega$. The numerical computation of (8), which accounts for the bulk of the computation time of our numerical method, is detailed in §3.3.

In this paper, the stencil $\mathcal{V}_h^x$ is obtained by rescaling and translating one of the instances shown in Figure 1. This is adequate because the anisotropies encountered in seismology are rather mild in absolute terms, even for crystal materials; in contrast, a data adaptive construction is preferred for applications involving much stronger anisotropies [Mir14b, Mir14a]. The discretization principle (8) is often referred to as semi-Lagrangian, in contrast with purely Eulerian finite difference approximations of the eikonal equation such as [Set96, Mir18, Mir19].

The numerical approximation of the arrival time (6) is defined as the unique solution $u : \Omega_h \to \mathbb{R}$ to the discrete system

$$u(x) = \Lambda_h u(x) \tag{9}$$

for all $x \in \Omega_h \setminus \{x_0\}$, and $u(x_0) = 0$ at the source point. Both the eikonal equation and its discretization (8) benefit from comparison principles, see Proposition D.2 in the latter case. From these, and under mild technical assumptions, one proves that there exists a unique discrete solution u_h to (9) on Ω_h, for each $h > 0$, which converges uniformly as $h \to 0$ to the unique viscosity solution of (2). This approach is standard and not detailed here, see [BR06].

The solution to the discrete non-linear system (9) may be computed using fixed point iterations, see Proposition D.3, or using any of the iterative methods considered in the introduction, such as the fast sweeping method [TCO04]. However, we advocate the fast marching method [Tsi95] in this paper, see Algorithm 1, which benefits from a number of advantages listed in the introduction. For that purpose, a careful choice of the stencil $\mathcal{V}_h^x$ is needed, as described in the next subsection.

Algorithm 1 The fast marching method (FMM)

Initialize: $u(x_0) = 0$, and $u(x) = +\infty$ for all $x \in \Omega_h \setminus \{x_0\}$. Tag all points as non-accepted.
While a non-accepted point remains: 1.
  Denote by y the non-accepted point minimizing $u(y)$. 2.
  Tag y as accepted. (Optionally, for e.g. higher order methods: PostProcess(y)). 3.
  For each non-accepted point x such that $y \in \mathcal{V}_h^x$: 4.
    $u(x) \leftarrow \tilde{\Lambda} u(x)$ (modified operator using only the values from accepted points). 5.

2.3 Acuteness and causality

In this subsection, we establish a property of the numerical scheme, known as *causality*. It can be informally rephrased as follows: the arrival times (a.k.a the values of the solution to (9)) earlier than some value τ, dictate the arrival times earlier than $\tau + \delta_1$, where δ_1 is a positive constant. An abstract formulation of causality is presented in Proposition D.1, and we show in Proposition D.3 that it enables solving the system (9) in finitely many fixed point iterations; see [Mir19, Proposition A.2] for the proof that this system is correctly solved by the FMM, Algorithm 1. Our definition of causality follows [SV01, AM12, Mir14a, Mir14b, Mir19] and is meant to enable the FMM. In the literature related to fast sweeping methods, causality is often given a different (non-equivalent) meaning, related to upwindness, stability, and to the monotony property in Proposition D.1.

Following [SV01], causality is derived from a geometrical *acuteness* property of the norms and discretization stencils, see Proposition 2.3. Finally, we discuss whether this property holds for various choices of norms and stencils. For that purpose, we introduce the central object of this section, which could be described as the angular width of the facets of a stencil measured with respect to a norm. The unoriented angle $\sphericalangle(u, v) \in [0, \pi]$ between two vectors $u, v \in \mathbb{R}^d \setminus \{0\}$ is defined as

$$\sphericalangle(u, v) := \arccos\big(\frac{\langle u, v\rangle}{\|u\|\|v\|}\big). \tag{10}$$

Definition 2.1. *Let N be a norm on $\mathbb{R}^d$, differentiable on $\mathbb{R}^d \setminus \{0\}$, and let $\mathcal{V}$ be a polygonal neighborhood of the origin. We let*

$$\Theta(N, \mathcal{V}) := \max\{\sphericalangle(\nabla N(v), w);\ v, w \text{ in a common facet of } \partial\mathcal{V}\}.$$

The differentiability assumption in Definition 2.1 is not essential, and could be removed as in [Mir14b]. It is however not restrictive for the application considered in this paper, which does involve differentiable norms, see Lemma 3.8.

The next definition accounts for the distortion of lengths by an anisotropic norm, thus completing Definition 2.1 which is related to the distortion of angles. The length distortion of a norm is also referred to as the strength of its anisotropy, and corresponds to the ratio between the highest and lowest value of the norm with respect to the orientation.

Definition 2.2 (Length distortion)**.** *For any norm N on $\mathbb{R}^d$, define*

$$\mu_*(N) := \min_{v\neq 0} \frac{N(v)}{\|v\|}, \qquad \mu^*(N) := \max_{v\neq 0} \frac{N(v)}{\|v\|}, \qquad \mu(N) := \frac{\mu^*(N)}{\mu_*(N)}.$$

The following proposition, which has numerous variants to be found in [Tsi95, KS98, SV01], governs the applicability of the fast marching method.

Proposition 2.3 (Acuteness implies causality)**.** *Let N and $\mathcal{V}$ be as in Definition 2.1. Let $\mathcal{I}_\mathcal{V}$ be the linear interpolation operator on $\partial\mathcal{V}$, and let u be a map defined at the vertices of $\mathcal{V}$. Define*

$$\lambda = \min_{y\in\partial\mathcal{V}} \mathcal{I}_\mathcal{V}\, u(y) + N(x - y) \tag{11}$$

and assume that the minimum is attained at a point $y = \alpha_1 y_1 + \cdots + \alpha_d y_d \in \partial\mathcal{V}$, where $y_1, \cdots, y_d$ are the vertices of a common facet of $\mathcal{V}$, and $\alpha_1, \cdots, \alpha_d$ are the barycentric coordinates. If $\Theta(N, \mathcal{V}) \leq \pi/2$, then for any $1 \leq i \leq d$ such that $\alpha_i > 0$ one has

$$\lambda \geq u(y_i) + \|x - y_i\|\mu_*(N)\cos\Theta(N, \mathcal{V}). \tag{12}$$

A proof of Proposition 2.3 is presented in §3.3. If $\Theta(N, \mathcal{V}) < \pi/2$, then the update value λ is strictly larger than the neighbor values $u(y_i)$ which play an active role in its computation, in the sense that $\alpha_i > 0$. Adopting the notation of (8), assume that

$$\Theta(N_x, \mathcal{V}_h^x) < \pi/2 \tag{13}$$

for each $x \in \Omega_h$. Then the system (9) is strictly causal, a property that is reformulated in an abstract manner in Proposition D.1, and enables the FMM. Note that multi-pass iterative methods such as fast sweeping remain applicable even if (13) fails, see Appendix D for more discussion.

The next definition and proposition bound the angle $\Theta(N, \mathcal{V})$ in terms of the norm and stencil separately. When the strength of the anisotropy in a medium is sufficiently mild, as in the case of geological media, this estimate allows to select an adequate discretization stencil for fast marching, see Tables 1 and 2. In contrast, more pronounced anisotropies as considered in [Mir14b, Mir14a, MD20] call for a data-adaptive and anisotropic stencil construction.

Definition 2.4. *Let N and $\mathcal{V}$ be as in Definition 2.1. Define the angular distortion of the norm as*

$$\Theta(N) := \max_{v \neq 0} \measuredangle(\nabla N(v), v), \tag{14}$$

and the angular width of the stencil as

$$\Theta(\mathcal{V}) := \max\{\measuredangle(v, w);\ v, w \text{ in a common facet of } \partial\mathcal{V}\}.$$

In the next proposition we denote by O_d the group of $d \times d$ orthogonal matrices, which are characterized by the identity $R^{-1} = R^{\mathrm{T}}$. Given a norm N and $R \in O_d$, we define a rotated norm by $N \circ R(x) := N(Rx)$ for all $x \in \mathbb{R}^d$.

Proposition 2.5. *Let N and $\mathcal{V}$ be as in Definition 2.1. Then*

$$\Theta(N, \mathcal{V}) \leq \Theta(N) + \Theta(\mathcal{V}). \tag{15}$$

Besides, there exists $R \in O_d$ such that $\Theta(N \circ R, \mathcal{V}) = \Theta(N) + \Theta(\mathcal{V})$.

Proof. Given $u, v \in \mathbb{R}^d \setminus \{0\}$, one has $\measuredangle(\nabla N(u), v) \leq \measuredangle(\nabla N(u), u) + \measuredangle(u, v)$. Thus $\Theta(N, \mathcal{V}) \leq \Theta(N) + \Theta(\mathcal{V})$ by definition. Besides, observing that $\Theta(N \circ R) = \Theta(N)$ for any $R \in O_d$, one obtains the relation: $\Theta(N \circ R, \mathcal{V}) \leq \Theta(N) + \Theta(\mathcal{V})$.

Then, let $u \in \mathbb{R}^d \backslash \{0\}$ be such that $\Theta(N) = \measuredangle(\nabla N(u), u)$, and let v, w in a common facet of $\partial\mathcal{V}$ be such that $\Theta(v) = \measuredangle(v, w)$. Up to replacing N with $N \circ R$, for some $R \in O_d$, we may assume that $u = v$. Up to replacing $\mathcal{V}$ with its image $R'(\mathcal{V})$ by a rotation $R' \in R^d$, we may assume that w lies in the plane generated by u and $\nabla N(u)$, in such way that $\measuredangle(\nabla N(u), w) = \measuredangle(\nabla N(u), u) + \measuredangle(u, w)$. This shows that $\Theta(N \circ R \circ R'^T, \mathcal{V}) = \Theta(N \circ R, R'(\mathcal{V})) = \Theta(N) + \Theta(\mathcal{V})$, and concludes the proof. □

The angular width $\Theta(\mathcal{V})$ of several stencils is given in Table 1, as well as the angular distortion $\Theta(N)$ of the norm associated with some geological media, numerically computed from their Hooke elasticity tensor as given in [BC91] and a fine sampling of (unit) vectors v in (14). In two dimensions, the square stencil is suitable for all geological media of interest, since $\Theta(N) + \Theta(\mathcal{V}) < \pi/2$. In three dimensions, the cut-cube stencil can be used with olivine and stishovite media, while the more anisotropic mica medium requires the refined spiky-cube stencil, see Figure 1 and Table 2.

The angular distortion $\Theta(N)$ can also be estimated in terms of the length distortion $\mu(N)$ of a norm, as shown in the next proposition. Two estimates are presented: a worst case estimate

	Square	Cut-cube	Cube	Spiky-cube
$\Theta(\mathcal{V})$	$\pi/4 = 0.785\ldots$	$\pi/3 = 1.047\ldots$	$\mathrm{acos}(1/\sqrt{3}) = 0.955\ldots$	$\pi/4 = 0.785\ldots$

	Olivine	Stishovite	Mica
$\Theta(N)$	$0.265\ldots$	$0.341\ldots$	$0.753\ldots$

Table 1: Angular width of the stencils illustrated on Figure 1, and angular distortion of the norm associated with several geological media. For completeness, the corresponding Hooke tensors (in GPa units, using Voigt notation) and densities are reproduced below from [BC91].

$$\begin{pmatrix} 323.7 & 66.4 & 71.6 & 0 & 0 & 0 \\ 66.4 & 197.6 & 75.6 & 0 & 0 & 0 \\ 71.6 & 75.6 & 235.1 & 0 & 0 & 0 \\ 0 & 0 & 0 & 64.6 & 0 & 0 \\ 0 & 0 & 0 & 0 & 78.7 & 0 \\ 0 & 0 & 0 & 0 & 0 & 79.0 \end{pmatrix}, \quad \rho = 3.311\mathrm{g/cm}^3 \text{ (Olivine)}$$

$$\begin{pmatrix} 453 & 211 & 203 & 0 & 0 & 0 \\ 211 & 453 & 203 & 0 & 0 & 0 \\ 203 & 203 & 776 & 0 & 0 & 0 \\ 0 & 0 & 0 & 252 & 0 & 0 \\ 0 & 0 & 0 & 0 & 252 & 0 \\ 0 & 0 & 0 & 0 & 0 & 302 \end{pmatrix}$$

(Stishovite) $\rho = 4.29\mathrm{g/cm}^3$,

$$\begin{pmatrix} 178 & 42.4 & 14.5 & 0 & 0 & 0 \\ 42.4 & 178 & 14.5 & 0 & 0 & 0 \\ 14.5 & 14.5 & 54.9 & 0 & 0 & 0 \\ 0 & 0 & 0 & 12.2 & 0 & 0 \\ 0 & 0 & 0 & 0 & 12.2 & 0 \\ 0 & 0 & 0 & 0 & 0 & 12.2 \end{pmatrix}, \quad \rho = 2.79\mathrm{g/cm}^3 \text{ (Mica)}$$

	Square	Cut-cube	Cube	Spiky-cube
Elliptic	iff $\mu \leq 1+\sqrt{2}$	iff $\mu \leq \sqrt{3}$	iff $\mu \leq (1+\sqrt{3})/\sqrt{2}$	iff $\mu \leq 1+\sqrt{2}$
Anelliptic	if $\mu \leq \sqrt{2}$	if $\mu \leq 2/\sqrt{3}$	if $\mu \leq \sqrt{3/2}$	if $\mu \leq \sqrt{2}$
Olivine, Stishovite, Mica	✓✓✓	✓✓×	✓✓×	✓✓✓

Table 2: Condition under which a norm N and stencil $\mathcal{V}$ satisfy $\Theta(N) + \Theta(\mathcal{V}) \leq \pi/2$, in terms of the length distortion $\mu = \mu(N)$. Note that the bound is sharp for elliptic norms (if and only if), but only sufficient for anelliptic norms, see Proposition 2.6. Stencils illustrated on Figure 1. Numerical values for the first two lines : $(2.41, 1.73, 1.93, 2.41)$ and $(1.41, 1.15, 1.22, 1.41)$.

in the anelliptic case in §B.1, and a sharp estimate in the elliptic case. Note that, strictly speaking, norms defined by a Hooke tensor are anelliptic, but their anellipticity is not always very pronounced.

Proposition 2.6. *For any elliptic (resp. anelliptic) norm N one has*

$$(\mu(N) + \mu(N)^{-1}) \cos\Theta(N) = 2 \qquad (\textit{resp.} \quad \mu(N)\cos\Theta(N) \geq 1).$$

Definition 2.7 (Norms and elliptic norms)**.** *A norm is a function $N : \mathbb{R}^d \to \mathbb{R}$ such that for all $v, w \in \mathbb{R}^d$, (i) $N(v+w) \leq N(v)+N(w)$, (ii) $N(\lambda v) = \lambda N(v)$ for all $\lambda \geq 0$, (iii) $N(-v) = N(v)$, and (iv) $N(v) \geq 0$ with equality iff $v = 0$. It is said* elliptic *if $N(v) = \sqrt{\langle v, Mv\rangle}$ for all $v \in \mathbb{R}^d$, where $M \in S_d^{++}$ is a positive definite matrix.*

The results presented in this subsection also apply if the symmetry assumption (iii) is removed in Definition 2.7. Norms lacking symmetry, often referred to as *quasi*-norms, define quasi-distances which can also be characterized by an eikonal equation and numerically computed using the fast marching method or another iterative method, with straightforward applications of the formalism presented in this paper, see [Mir14b] in two dimensions.

Causality for TTI metrics with the use of fixed stencils. We illustrate the causality property for our stencils on the specific case of TTI anisotropy, but bear in mind that our method can similarly handle anisotropy coming from a Hooke tensor of general complexity.

The Thomsen parameters [Tho86] denoted $(V_p, V_s, \epsilon, \delta)$, often complemented with a rotation R, define the TTI eikonal equation of the form

$$a p_r^4 + b p_z^4 + c p_r^2 p_z^2 + d p_r^2 + e p_z^2 = 1 \tag{16}$$

where $p_r^2 = p_x^2 + p_y^2$ and $(p_x, p_y, p_z) = R\nabla u$, with parameters (a, b, c, d, e):

$$\begin{cases} a &= -(1+2\varepsilon)V_p^2 V_s^2, \\ b &= -V_p^2 V_s^2, \\ c &= -(1+2\varepsilon)V_p^4 - V_s^4 + (V_p^2 - V_s^2)(V_p^2(1+2\delta) - V_s^2), \\ d &= V_s^2 + (1+2\varepsilon)V_p^2, \\ e &= V_p^2 + V_s^2. \end{cases}$$

The PDE (16) suffers from an ambiguity, similar to (3), in the sense that two propagation speeds are solution, in each direction. In this paper, we only consider the fastest propagation speed, corresponding to pressure waves. From Thomsen parameters and the rotation one can define a Hooke tensor such that (3) is equivalent to (16).

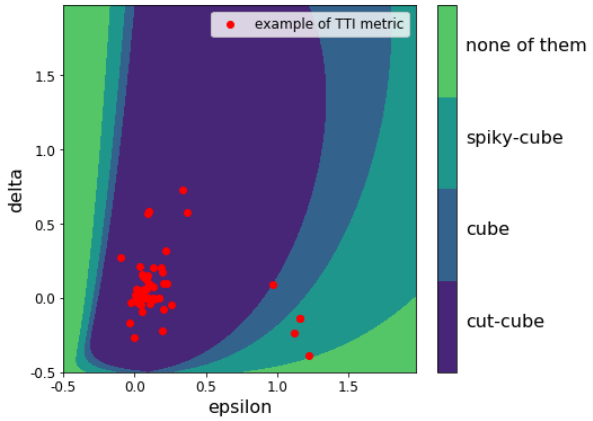

Figure 2: Acuteness property, depending on the stencil and Thomsen parameters.

We use the criterion of Proposition 2.3 to determine whether our fixed 3D stencils provide a causal scheme depending on the Thomsen parameters. With Proposition 2.5, we make our criterion independent from the rotation chosen for the TTI metric. Therefore, we only need to determine the length distortion for a set of Thomsen parameters $(V_p, V_s, \epsilon, \delta)$.

We set $V_s = 0$ for an easier visualization of the results[2]. Besides, we can set $V_p = 1$ with no loss of generality. Results are shown in Figure 2, depending on parameters (ϵ, δ). We also plotted the (ϵ, δ) values from 58 examples of media presented in [Tho86]. Out of the 58 media, only 4 of them are such that the cut-cube stencil does not guarantee a causal scheme: these four media are the "Muscovite crystal", "Biotite crystal", "Gypsum-weathered material" and "Aluminum-lucite composite". From these 4 media, only the "Biotite crystal" is such that the spiky-cube stencil does not guarantee a causal scheme. We conclude that the cut-cube stencil suffices to enable the FMM with most practical cases of seismic anisotropy.

2.4 Source factorization, and high order finite differences

We describe enhancements of the numerical scheme (8), aimed at achieving higher accuracy, via an additive factorization of the source singularity, and the use of higher order upwind finite differences, in the spirit of [LQ12, TH16] and [Set99] respectively. For that purpose, we rely on an infinitesimal variant of Bellman's optimality principle (7):

$$0 = \min_{y \in \partial \mathcal{V}} \langle \nabla u(x), y - x \rangle + N_x(x - y), \tag{17}$$

where $\mathcal{V}$ is a neighborhood of a point $x \in \Omega$. This property can be derived from (7), or alternatively from the eikonal equation (2) and the relation $N_x^*(p) = \max\{\langle p, v \rangle;\ N_x(v) \leq 1\}$ which follows from (5) and Legendre-Fenchel duality. In general, (17) should be understood in the sense of viscosity solutions [BCD08], but for the sake of simplicity we assume in this discussion that u is differentiable at x.

Equation (17) is discretized in a fashion similar to (8) and (9):

$$0 = \min_{y \in \partial \mathcal{V}_h^x} \mathcal{I}_h^x D(u, x, y - x) + N_x(x - y), \tag{18}$$

[2]Note that the Thomsen parameter V_s does not exactly correspond to the physical speed of the S-wave, and so V_s does have an impact on the value of the first arrival time, as well as the geometry and anisotropy of the equivalent Hooke tensor. However, on usual values for geophysical media, the impact of V_s is very small so the visualisation of Figure 2 is not significantly altered.

where $D(u, x, y-x)$ is a finite-difference approximation of $\langle \nabla u(x), y-x \rangle$, defined for $x, y \in \Omega_h$. Recall that $\mathcal{I}_h^x$ denotes, as in (8), the linear interpolation operator on the polygonal stencil boundary $\partial \mathcal{V}_h^x$, whose vertices lie in Ω_h. For convenience, we also let $D_h^x u(v) := D(u, x, hv)/h$, where $v = (y-x)/h$, which approximates of the directional gradient $\langle \nabla u(x), v \rangle$. The original scheme (8) is recovered by letting

$$D_h^x u(v) = \frac{u(x+hv) - u(x)}{h} \qquad \Big(\text{equivalently } D(u, x, y-x) := u(y) - u(x)\Big). \tag{19}$$

Substantial improvements in accuracy can however be obtained using more complex finite difference schemes which (i) factor the solution singularity at the source point x_0, and (ii) increase the finite difference order. Note that increased accuracy is suggested by a consistency analysis, and observed numerically §4. However, from the theoretical standpoint, we cannot guarantee that these modifications improve numerical accuracy, but only that they do not significantly degrade it, see Appendix D.

Additive source factorization. The solution to the eikonal equation (2) is non-differentiable at the source point x_0. As a result, the finite difference approximation of its derivatives, as in (19), is inaccurate for x close to x_0, which degrades the accuracy of the numerical results. Source factorization methods [LQ12] subtract to the unknown u a known function u_* which has same singularity as the solution, but whose value and derivatives can be numerically evaluated to machine precision at a modest cost. The following choices are considered: assuming w.l.o.g. that $x_0 = 0$

$$u_1(x) := N_0(x), \qquad u_2(x) := \frac{1}{2}(N_0(x) + N_x(x)). \tag{20}$$

The factor u_2 is considered for the first time in this paper. As illustrated in the numerical experiments §4, it is more accurate than u_1, and is necessary to achieve third order accuracy.

Following the additive source factorization method [LQ12], and denoting by u_* the chosen factor (u_1 or u_2), we introduce the corrected finite difference operator

$$D_h^x u(v) = \frac{u(x+hv) - u(x)}{h} + \left(\langle \nabla u_*(x), v \rangle - \frac{u_*(x+hv) - u_*(x)}{h} \right). \tag{21}$$

The resulting modified scheme (18) is only a small perturbation of the original one (9), featuring corrective terms (21, right) of magnitude $\mathcal{O}(h^2/\|x - x_0\|)$. If the original scheme was strictly causal (13), then this perturbation also is, except possibly on a neighborhood of radius $\mathcal{O}(h)$ of the source x_0 where (20) is in any case an excellent approximation of the solution u. As a result, the modified scheme can be solved in a single pass, using the Fast Marching algorithm, see Proposition D.4 and the discussion below.

High order finite differences. High order finite differences advantageously replace first order ones (19, left) in places where the solution is smooth. These differences should be upwind, i.e. one sided, so as to respect the causality principle underlying the eikonal equation. Second order upwind finite differences for instance read

$$D_h^x u(v) = \frac{u(x+hv) - u(x)}{h} - \frac{u(x+2hv) - 2u(x+hv) + u(x)}{2h}, \tag{22}$$

and third order differences incorporate the additional term

$$\frac{u(x+3hv) - 3u(x+2hv) + 3u(x+hv) - u(x)}{3h}. \tag{23}$$

Note that this approach requires a Cartesian grid discretization, in such way that $x + 2hv$ and $x + 3hv$ are points of the discretization grid $h\mathbb{Z}^d$, in addition to x and $x + hv$. Alternative approaches to high order finite differences also exist, see e.g. [BLZ10]. Source factorization can easily be combined with high order finite differences: similarly to (21), symbolically compute the directional gradient $\langle \nabla u_*(x), v \rangle$ of the factor (20), and remove its finite difference approximation $D_h^x u_*(v)$.

In contrast with source factorization, the use of high order finite differences breaks the fundamental result of Proposition 2.3 on causality, as well as discrete comparison principles (the modified scheme is not monotone). For this reason, they should be used with caution. In practice, following [Set99], we introduce them in the post processing step of the Fast Marching method, see Line 3. of Algorithm 1. At this stage the numerical scheme is re-evaluated at the accepted point y using high order finite differences, provided they (i) only involve accepted values, and (ii) are close enough to the standard first order differences. This avoids introducing instabilities in the FMM, and guarantees that the accuracy is not worse than the first order scheme, see Proposition D.5 and the discussion above.

2.5 Summary of the numerical method

This paper defines a numerical method, designed to solve the eikonal equation on a geological medium defined with a fully general Hooke tensor (21 parameters). In this subsection, we present a summary of each of its steps. Computer code which implements the method in this study can also be found at: `https://github.com/Mirebeau`, with illustrative Python Notebooks.

Choice of discretization stencils. In order to enable the FMM, which we advocate in this paper since it yields the fastest computation times, the stencils need to be acute w.r.t. the metric, see (13). Some results presented in this paper allow to infer the choice of stencils from possibly known geometric properties of the metric: the angular distortion in Proposition 2.5, and the length distortion in Proposition 2.6. More specific examples are also considered: materials described in terms of Thomsen parameters in Fig. 2, and a selection of minerals in Table 2. Typically, the cut-cube stencil is acute for most metrics from geological media.

Numerical solver. Once acute stencils are set, the discrete system (9) can be solved in a single pass by the FMM, whose in implementation is detailed in Algorithm 1. (Alternatively, if the stencils are not acute, an iterative method such as fast sweeping may be used, see Appendix D.) For better accuracy, we also use a source factorization, as well as high order finite differences, see §2.4.

Computation of the update operator. The FMM requires the computation of the update operator Λ from Definition 8, which is used to compute the arrival time at any position as a minimization problem over arrival times estimated on the facets of the stencil at this position. The computation of the update operator is the most expensive aspect of our numerical method. The minimum is computed on the vertices, edges and faces of the stencil: details of the implementation can be found in §3.4.

3 Numerical computation of the norm and update operator

We provide in this section the implementation details for the numerical computation of the norm associated with a given Hooke tensor, which is a basic ingredient of our numerical solver of the

eikonal equation (2). We also establish Proposition 2.3 in §3.3, on causality property of the update operator, and discuss its numerical evaluation in §3.4. Throughout this section we fix a Hooke tensor c, and define $m_c(p) \in S_d$ and $N^*(p)$ for all $p \in \mathbb{R}^d$

$$m_c(p)_{ik} := \sum_{j,l} c_{ijkl}\, p_j\, p_l, \qquad\qquad N_c^*(p) := \sqrt{\|m_c(p)\|}, \tag{24}$$

where the spectral norm (largest eigenvalue) is used in (24, right). This definition is similar to (1), except for the density which is ignored for simplicity, w.l.o.g. up to rescaling the Hooke tensor. The primal norm N_c is defined as maximization of a linear form subject to a non-linear convex constraint, similar to (5): for all $v \in \mathbb{R}^d$

$$N_c(v) := \max\{\langle p, v\rangle;\ N_c^*(p) \leq 1\}. \tag{25}$$

We rely on SQCQP (sequential quadratically-constrained quadratic programming) to address this problem numerically, see Appendix C, of which a variant also arises in the evaluation of the update operator (8), see §3.4. For this method, the constraint needs to take the form "$f \leq 0$" (resp. "$f \geq 0$") (or another constant bound) where the function f is both:

(a) Strongly convex (resp. strongly concave), see Definition 3.4.

(b) Efficiently evaluated numerically, as well as its gradient and hessian.

The constraint $N_c^* \leq 1$ in (25) fails both of these properties. Considering $(N_c^*)^2 \leq 1$ fixes (a), see Theorem 3.3, but not (b) since $N_c^*(p)$ involves the spectral norm $\|m_c(p)\|$ which is itself the root of a degree three polynomial. We thus consider alternative expressions of the constraint, and denote

$$B_c^* := \{p \in \mathbb{R}^d; N_c(p) \leq 1\}, \qquad\qquad f_c(p) := \det(\mathrm{Id} - m_c(p)), \tag{26}$$

We prove in Proposition 3.7 below, under suitable assumptions, that B_c^* is the connected component of the origin in the set $\{f_c \geq 0\}$.

We can thus replace the highly non-linear constraint $N_c^*(p) \leq 1$ with the constraint $f_c(p) \geq 0$. Since f_c is a polynomial (of degree $2d$ in d variables, inhomogeneous), it complies with (b). However, f_c is in general not concave, thus fails (a), see nevertheless Remark 3.11. For this reason we consider yet other alternative expressions of the constraint:

$$f_c^{\frac{1}{d}} \geq 0 \tag{27}$$

and, for $\alpha \geq 0$,

$$\exp[-\alpha f_c] \leq 1. \tag{28}$$

The function $f_c^{\frac{1}{d}}$ used in (27) is a barrier function for the set B_c^*: it is strictly positive in its interior, cancels on its boundary, and is strongly concave, see Theorem 3.3. However, it is not defined outside of B_c^*, hence its use is restricted to optimization procedures using only interior points, which is not the case of SQCQP. Even so, it is natural to consider this expression of the constraint before moving to (28), see proof of Theorem 3.3.

One the other hand, the function $\exp[-\alpha f_c]$ is smooth, defined over the whole of $\mathbb{R}^d$, and easy to evaluate thus complies with (b). The main result of this section, Theorem 3.3, establishes that it is strongly convex on a neighborhood of B_c^*, thus also complies with (a), when α is sufficiently large. See Remark 3.11 on the effective choice of this constant. This reformulation of

the constraint is thus suitable for applying the SQCQP optimization routine to compute $N_c(v)$, see Appendix C. For numerical stability, the exponential is taken into account in the optimization via Remark C.3.

In order to state our results, we need to introduce some definitions. Recall that a Hooke tensor is a 4th-order tensor $c = (c_{ijkl})$, $i, j, k, l \in \{1, \cdots, d\}$, obeying the symmetry relations $c_{ijkl} = c_{klij} = c_{jikl}$. Given two symmetric matrices m_1, m_2, we write $m_1 \succeq m_2$ (resp. $m_1 \succ m_2$) if $m_1 - m_2$ is positive semi-definite (resp. positive definite); this is known as the Loewner order.

Definition 3.1. *A Hooke tensor c is said* elliptic *(resp.* strictly elliptic*) iff $m_c(p)$ is positive semi-definite (resp. positive definite) for each $p \in \mathbb{R}^d \setminus \{0\}$.*

We let c_{ell} be the largest constant such that $m_c(p) \succeq c_{\text{ell}} \operatorname{Id} \|p\|^2$ for all $p \in \mathbb{R}^d$, and note that $c_{\text{ell}} \geq 0$ (resp. $c_{\text{ell}} > 0$) if c is elliptic (resp. strictly elliptic).

Definition 3.2. *A Hooke tensor c is said* separable *iff the largest eigenvalue of $m_c(p)$ has multiplicity one for all $p \neq 0$.*

A Hooke tensor is separable, in the sense of Definition 3.2, iff the pressure waves are strictly faster than the other modes of propagation (e.g. P-SV-waves), which is typical of the materials encountered in seismology. The notion of Hooke tensor ellipticity is further discussed in Remark 3.5, and is unrelated with elliptic anisotropy, see Definition 2.7.

Theorem 3.3. *Let c be a strictly elliptic Hooke tensor. Then (i) N_c^* is a norm, and $(N_c^*)^2$ is $2c_{\text{ell}}$-convex, (ii) $f_c^{\frac{1}{d}}$ is $2c_{\text{ell}}$-concave in B_c^*, (iii) if in addition c is separable, and α is large enough, then $\exp[-\alpha f_c]$ is strongly convex in a neighborhood of B_c^**

A property closely related to point (i) is established in [Mus03], with a different proof.

Definition 3.4. *A function f, defined on a convex domain $\Omega \subset \mathbb{R}^d$, is said δ-convex iff for all $p, q \in \Omega$ and all $t \in [0, 1]$ one has*

$$f((1-t)p + tq) \leq (1-t)f(p) + tf(q) - \frac{\delta}{2} t(1-t)\|p - q\|^2. \tag{29}$$

A 0-convex function is simply said convex, and a δ-convex function for some $\delta > 0$ is said strongly convex. A function f is said δ-concave iff $-f$ is δ-convex. If f is twice continuously differentiable, then δ-convexity is equivalent to the property $\nabla^2 f \succeq \delta \operatorname{Id}$. If f_1 and f_2 are δ-convex, then $f = \max\{f_1, f_2\}$ also is.

The following variant of the parallelogram identity, which has obvious ties to (29), is used twice in the proof of Theorem 3.3: for any quadratic form A, any points p, q, and any $t \in \mathbb{R}$

$$A((1-t)p + tq) = (1-t)A(p) + tA(q) - t(1-t)A(p-q). \tag{30}$$

Remark 3.5 (Hooke tensor positivity)**.** *Following [BST83], a Hooke tensor is said elliptic (resp. positive) if for all $p, q \in \mathbb{R}^d$ (resp. $m \in S_d$) one has*

$$\sum_{i,j,k,l} c_{ijkl}\, p_i\, q_j\, p_k\, q_l \geq 0 \qquad \Big(\textit{resp.} \sum_{i,j,k,l} c_{ijkl}\, m_{ij}\, m_{kl} \geq 0\Big).$$

This notion of ellipticity is clearly equivalent with Definition 3.1. Note also that positivity implies ellipticity, as already observed in [BST83], by choosing $m_{ij} = \frac{1}{2}(p_i q_j + p_j q_i)$.

Remark 3.6 (Gradient of $N_c(v)$)**.** *Let c be a strictly elliptic Hooke tensor, let $v \in \mathbb{R}^d \setminus \{0\}$, and let p be optimal in* (25)*. Then $\nabla N_c(v) = p$ by the envelope theorem [Car01]. This observation allows to numerically implement source factorization, see* (20) *and* (21)*.*

We conclude the introduction of this section with a description of the constraint set B_c^* in terms of the level sets of f_c. Denote by $\mathrm{CC}_x(X)$ the connected component of a point x in a set X.

Proposition 3.7. *If c is elliptic and separable, then $B_c^* = \mathrm{CC}_0\{f_c \geq 0\}$.*

Proof. For all $p \in \mathbb{R}^d$, denote by $\lambda_1(p) \geq \cdots \geq \lambda_d(p)$ the eigenvalues of $m_c(p)$, which depend continuously on p. Note that $\lambda_d(p) \geq 0$ since c is elliptic, and that $\lambda_1(p) > \lambda_2(p)$ for all $p \neq 0$ since c is separable. Note also that $N_c(p) = \sqrt{\lambda_1(p)}$ and $f_c(p) = (1-\lambda_1(p)) \cdots (1-\lambda_d(p))$.

Proof of the direct inclusion: if $p \in B_c^*$, then $1 \geq \lambda_1(p)$. Therefore $f_c(\sigma p) = (1-\sigma^2\lambda_1(p)) \cdots (1-\sigma^2\lambda_d(p)) \geq 0$ for all $\sigma \in [0,1]$, thus $p \in \mathrm{CC}_0\{f_c \geq 0\}$ as announced.

Proof of the reverse inclusion: the sets $B_c^* = \{\lambda_1 \leq 1\}$ and $E := \{\lambda_2 \geq 1\}$ are closed, and disjoint by separability. Since $\{f_c \geq 0\} \subset B_c^* \sqcup E$, any connected component of $\{f_c \geq 0\}$ is entirely contained in either B_c^* or E. It follows that $\mathrm{CC}_0\{f_c \geq 0\} \subset B_c^*$ which concludes. □

3.1 Convexity and smoothness of the dual norm N_c^*

We establish point (i) of Theorem 3.3, and also discuss the smoothness and uniform convexity properties of N_c^*. Let c be an elliptic Hooke tensor. Then for any $p, q \in \mathbb{R}^d$ one has,

$$\|q\|_{m_c(p)}^2 = \sum_{i,j,k,l} c_{ijkl}\, q_i\, p_j\, q_k\, p_l = \|p\|_{m_c(q)}^2,$$

where $\|q\|_m := \sqrt{\langle q, mq\rangle}$. Therefore

$$N_c^*(p) := \sqrt{\|m_c(p)\|} = \max_{|q|=1} \|q\|_{m_c(p)} = \max_{|q|=1} \|p\|_{m_c(q)}. \tag{31}$$

Proof of point (i) of Theorem 3.3. The function $p \in \mathbb{R}^d \mapsto \|p\|_m$ is convex if m is a symmetric positive semi-definite matrix, and is a norm if m is positive definite. In the latter case, $p \mapsto \|p\|_m^2$ is δ-convex with parameter $\delta = 2\lambda_{\min}(m)$, as follows from the parallelogram identity (30). The announced result follows from (31), the stability of these properties under the max operation, and the observation that $\lambda_{\min}(m_c(q)) \geq c_{\mathrm{ell}}$ if $\|q\| = 1$. □

Lemma 3.8. *Let c be an elliptic and separable Hooke tensor. Then N_c^* is C^∞ smooth on $\mathbb{R}^d \backslash \{0\}$.*

Proof. By construction, $N_c^*(p)^2$ is the largest root of the polynomial $\lambda \mapsto \det(\lambda\,\mathrm{Id} - m_c(p))$, which by assumption is positive and simple (a.k.a. of multiplicity one). The result immediately follows from the regularity of a polynomial's simple roots with respect to variations in the coefficients. □

The strong convexity of $(N_c^*)^2$ and its C^∞ smoothness on $\mathbb{R}^d \setminus \{0\}$, see Theorem 3.3 and Lemma 3.8, imply the same properties of the norm N_c by Legendre-Fenchel duality.

3.2 Convexity of the alternative barriers for the dual unit ball

We conclude in this subsection the proof of Theorem 3.3.

Proof of point (ii) of Theorem 3.3. Each component of $p \mapsto m_c(p)$ is a quadratic form by (24, left), hence by the parallelogram identity (30) one has for any $p, q \in \mathbb{R}^d$ and any $t \in [0,1]$

$$m_c((1-t)p + tq) = (1-t)m_c(p) + tm_c(q) - t(1-t)m_c(p-q). \tag{32}$$

Recall that $\det^{\frac{1}{d}}$ is concave[3] over the cone S_d^+. By homogeneity, this implies super-additivity: $\det(A+B)^{\frac{1}{d}} \geq \det(A)^{\frac{1}{d}} + \det(B)^{\frac{1}{d}}$ for all $A, B \in S_d^+$. Using successively (32), the super-additivity and the concavity of $\det^{\frac{1}{d}}$ on S_d^+, we obtain for any $p, q \in B_c^*$, $t \in [0,1]$, and denoting $M[p] := \mathrm{Id} - m_c(p)$

$$\begin{aligned}\det(M[(1-t)p+tq])^{\frac{1}{d}} &= \det\big((1-t)M[p] + tM[q] + t(1-t)m_c(p-q)\big)^{\frac{1}{d}} \\ &\geq \det\big((1-t)M[p] + tM[q]\big)^{\frac{1}{d}} + t(1-t)\det\big(m_c(p-q)\big)^{\frac{1}{d}} \\ &\geq (1-t)\det(M[p])^{\frac{1}{d}} + t\det(M[q])^{\frac{1}{d}} + t(1-t)c_{\mathrm{ell}}\|p-q\|^2. \qquad \square\end{aligned}$$

Given a twice continuously differentiable function f, and constants $\alpha, \beta \in \mathbb{R}$, we recall the expression of the composite hessians,

$$\nabla^2 \exp(-\alpha f) = \big(\alpha \nabla f \nabla f^T - \nabla^2 f\big)\mu_1, \qquad \nabla^2(f^\beta) = \big(\frac{\beta-1}{f}\nabla f \nabla f^T + \nabla^2 f\big)\mu_2, \tag{33}$$

only defined where $f > 0$ for (33, right). We denoted $\mu_1 := \alpha \exp(-\alpha f)$ and $\mu_2 := \beta f^{\beta-1}$. Proposition 3.10 below and (33, left) together imply point (iii) of Theorem 3.3. Recall that the comatrix $\mathrm{co}(M)$ has polynomial entries in a matrix M, and satisfies $M^{-1} = \mathrm{co}(M)^{\mathrm{T}}/\det(M)$ when M is invertible.

Lemma 3.9. *Let $M \in S_d$ and $v \in \mathbb{R}^d$. Assume that $\langle w, Mw\rangle \geq c\|w\|^2$ for all $w \in v^\perp$, where $c > 0$. Then $M + \alpha v v^{\mathrm{T}} \succ 0$ iff $\alpha > \alpha_* := -\det(M)/\langle v, \mathrm{co}(M)v\rangle$. (Also, $\langle v, \mathrm{co}(M)v\rangle \geq c^{d-1}$.)*

Proof. Up to a linear change of coordinates, we may assume that $v = (1, 0, \cdots, 0)$. Denote by $\tilde{M} \in S_{d-1}$ the matrix extracted from M by omitting the first line and first column, which by assumption satisfies $\tilde{M} \succeq c\,\mathrm{Id}$. Then $\langle v, \mathrm{co}(M)v\rangle = \det \tilde{M} \geq c^{d-1}$ as announced. Also $\det(M + \alpha v v^T) = \det(M) + \alpha \det(\tilde{M}) = \det(M) + \alpha\langle v, \mathrm{co}(M)v\rangle$ is positive iff $\alpha > \alpha_*$.

Assume for contradiction that there exists a sequence $(w_n)_{n\geq 0}$ such that $\|w_n\| = 1$ and $\langle w_n, (M + nvv^T)w_n\rangle \leq 0$ for all $n \geq 0$. Up to extracting a subsequence we assume may that $w_n \to w_*$ as $n \to \infty$, where $\|w_*\| = 1$. Noting that $\langle w_n, v\rangle^2 \leq -\langle w_n, Mw_n\rangle/n \to 0$ as $n \to \infty$, we obtain that $\langle w_*, v\rangle = 0$. Then $0 \geq \langle w_n, (M + nvv^T)w_n\rangle \geq \langle w_n, Mw_n\rangle \to \langle w_*, Mw_*\rangle > 0$, as $n \to \infty$, which is a contradiction. We conclude that there exists n_* such that $M + n_* v v^T \succ 0$.

The set $I = \{\alpha \in \mathbb{R};\ M + \alpha v v^T \succ 0\}$ is the connected component of n_* in the set $J = \{\alpha \in \mathbb{R};\ \det(M + \alpha v v^T) > 0\}$. Noting that $J =]\alpha_*, \infty[$, we conclude the proof. $\square$

Proposition 3.10. *Let c be a strictly elliptic and separable Hooke tensor. Then there exists a constant $\alpha \geq 0$ such that $g(\alpha, p) := \alpha \nabla f_c(p) \nabla f_c(p)^T - \nabla^2 f_c(p)$ is positive definite for all p in a neighborhood of B_c^*.*

Proof. Let $p \in \mathrm{int}(B_c^*)$. By point (ii) of Theorem 3.3 and (33, right) one has $g(\alpha(p), p) \succ 0$ with $\alpha(p) := (1 - 1/d)/f(p)$.

Let $p \in \partial B_c^*$, and let $\lambda_1 \geq \cdots \geq \lambda_d$ be the eigenvalues of $m_c(p)$. One has $\lambda_1 = 1$ since $p \in \partial B_c^*$, and $\lambda_2 < 1$ by separability. Therefore $f_c((1+\varepsilon)p) = \det(\mathrm{Id} - (1+\varepsilon)^2 m_c(p)) = -2\varepsilon(1-\lambda_2)\cdots(1-\lambda_d) + \mathcal{O}(\varepsilon^2)$, which shows that $v := \nabla f_c(p)$ is nonzero. On the other hand, the strong convexity of $(N_c^*)^2$, and the fact that the level sets $N_c^* = 1$ and $f_c = 0$ coincide,

[3] There are countless proofs of this fact, related to the Brunn-Minkowski theorem. For instance, a reduction shows that one can suppose that one matrix is the identity and the other is diagonal, in which case the inequality follows from the convexity of $t \in \mathbb{R} \mapsto \ln(1 + e^t)$.

implies that $\langle w, \nabla^2 f_c(p) w \rangle < 0$ for all $w \in v^\perp$. From these properties and Lemma 3.9 we obtain that $g(\alpha(p), p) \succ 0$ for sufficiently large $\alpha(p)$.

The announced result follows from the compactness of B_c^*, the continuity of ∇f_c and $\nabla^2 f_c$ and openness of S_d^{++}, and the existence of a suitable $\alpha = \alpha(p)$ at each $p \in B_c^* = \mathrm{int}(B_c^*) \cup \partial B_c^*$ as shown above. □

Remark 3.11 (Effective value of α)**.** *Proposition 3.10 produces the constant α by a compactness argument, which is not quantitative. We numerically approximated this constant, using Lemma 3.9 and a fine sampling of B_c^*, for a variety of materials, and found for example that $\alpha = 40$ is suitable for the Hooke tensor derived from the mica material, and $\alpha = 62$ is suitable for the Hooke tensor derived from the stishovite material (as defined in Table 1).*

Numerical computation of $N_c(v) = \max\{\langle p, v\rangle; \exp[-\alpha f_c(p)] \leq 1\}$ is implemented using the SQCQP method, described in Appendix C and using Remark C.3 to avoid overflow and underflow error associated with the evaluation of $\exp[-\alpha f_c]$. Our experiments eventually led to the observation that SQCQP is robust and rather insensitive to the parameter α. In particular and to our surprise, no failure of this iterative optimization procedure was observed when letting $\alpha \to 0$, which amounts to applying SQCQP with the constraint $f_c \geq 0$: the point $p = 0$ appears to remain in the basin of attraction of the solution, even though the constraint function is non-concave. Explaining this fortunate behavior is beyond the scope of the current work.

3.3 Proof of the causality property

This subsection is devoted to the proof of Proposition 2.3, which relates a geometrical property of the stencils with a causality of the update operator (8) of the Fast Marching method. For that purpose, let us recall that this operator is defined as a minimization problem over a triangulated surface: the boundary $\partial \mathcal{V}_h^x$ of the discretization stencil, see (8). For each k-dimensional facet of this surface, we thus solve an optimization problem of the following form

$$\lambda = \min_{\xi \in \Xi_k} \langle l, \xi \rangle + N(V\xi), \qquad \text{where} \quad \Xi_k := \{\xi \in [0, \infty[^{k+1}; \langle \xi, \mathbb{1}_k \rangle = 1\}, \tag{34}$$

where $\mathbb{1}_k := (1, \cdots, 1) \in \mathbb{R}^{k+1}$. We denoted by N a norm on $\mathbb{R}^d$, assumed to be differentiable on $\mathbb{R}^d \setminus \{0\}$, and by V a matrix of shape $d \times (k+1)$. Note that the norm N and the set Ξ_k are convex, hence this problem is amenable to numerical optimization, see §3.4. In the context of (8), $N = N_x$, the matrix V collects the vertices of the k-facet of interest of $\partial \mathcal{V}_x^h$, and the vector l collects the values of the unknown u at the vertices of the facet.

Lemma 3.12. *Assume that the minimum (34, left) is attained at a point ξ of the relative interior of Ξ_k. Then denoting $p = \nabla N(V\xi)$ one has*

$$\lambda \mathbb{1}_k = l + V^{\mathrm{T}} p, \qquad N^*(p) = 1 \tag{35}$$

Proof. Equation (35, right) follows from $p = \nabla N(V\xi)$ and Legendre-Fenchel duality. The Karush-Kuhn-Tucker relations for the optimization problem (34), given that the non-negativity constraints are inactive, yield (35, left) with an arbitrary Lagrange multiplier λ' which in principle needs not coincide with the value λ of the optimization problem (34). Their equality is established as follows:

$$\lambda' = \lambda' \langle \xi, \mathbb{1}_k \rangle = \langle \xi, l + V^{\mathrm{T}} p \rangle = \langle l, \xi \rangle + \langle p, V\xi \rangle = \langle l, \xi \rangle + N(V\xi) = \lambda. \qquad \square$$

The next result links the acuteness of the stencil with the causality of the numerical scheme, following [Tsi95, KS98, SV01]. For that purpose we denote, for each matrix V of shape $d \times (k+1)$

$$\Theta(N, V) := \max_{\xi, \xi' \in \Xi_k} \sphericalangle(\nabla N(V\xi), V\xi'). \tag{36}$$

Proposition 3.13 (Acuteness implies causality, single facet version)**.** *Assume that the minimum (34, left) is attained at a point ξ in the relative interior of Ξ_k, and that $\Theta(N, V) \leq \pi/2$. Denote by $l_0, \cdots, l_k$ the components of l, and by $v_0, \cdots, v_k$ the columns of V. Then for any $0 \leq i \leq k$*

$$\lambda \geq l_i + \|v_i\| \mu_*(N) \cos \Theta(N, V) \tag{37}$$

Proof. Considering (35, left) componentwise, we obtain $\lambda = l_i + \langle v_i, p \rangle$. Since v_i and $V\xi$ belong to the same facet of the stencil, one obtains using the angle condition and Lemma B.1

$$\begin{aligned} \langle v_i, p \rangle = \langle v_i, \nabla N(V\xi) \rangle &\geq \|v_i\| \|\nabla N(V\xi)\| \cos \Theta(N, V) \\ &\geq \|v_i\| \mu_*(N) \cos \Theta(N, V). \end{aligned}$$

□

Proof of Proposition 2.3. Up to renumbering the vertices, and eliminating those whose barycentric coordinate vanishes, we assume that the minimum of (11) is attained at a point $y = \alpha_0 y_0 + \cdots + \alpha_k y_k$, where $\alpha_i > 0$ for all $0 \leq i \leq k$, and $y_0, \cdots, y_k$ are the vertices of minimal facet of $\partial\mathcal{V}$ containing y. (The dimension of this facet is k, with $0 \leq k < d$.) Denote by V the matrix of columns $y_0 - x, \cdots, y_k - x$, and let $l = (u(y_0), \cdots, u(y_k))$. Then (37) yields (12), since in view of Definition 2.1 one has $\Theta(N, V) \leq \Theta(N, \mathcal{V})$. This concludes the proof. □

3.4 Numerical computation of the update operator

The core of our numerical solver of the eikonal equation is devoted to the numerical computation of the update operator (8), defined by the minimization problem

$$\min_{y \in \partial\mathcal{V}_h^x} \mathcal{I}_h^x u(y) + N_x(x - y).$$

Since the stencil boundary $\partial\mathcal{V}_h^x$ is a triangulated surface, see Fig. 1, we can minimize over each facet separately. Optimization over a single given facet takes the form (34), which is a mathematically well posed problem: the minimization of a convex functional over a simplex. However efficient numerical implementation bears importance, as it dominates the computational cost of our method. A first optimization, specific to the FMM, is to consider only the facets of $\mathcal{V}_h^x$ containing the point y that was last accepted, and triggered the update see Algorithm 1. Indeed the values of u associated to the other vertices of $\mathcal{V}_h^x$ have not changed since the previous update at x.

We discuss here the key ingredients of the implementation of (34), for a norm $N = N_c$ associated with a Hooke tensor c. We focus on the case of a three dimensional stencil ($d = 3$) and distinguish cases depending on the dimensionality k of the sub-facet: a vertex (0-facet), an edge (1-facet), or a face (2-facet) which must be a triangle.

Vertex (k=0). The optimization problem (34) associated with a vertex v_0 is simplified into the trivial expression $\lambda = N_c(v_0) + l_0$. The edge length $N_c(v_0)$ is numerically evaluated as described in the introduction of this section.

Edge (k=1). The optimization problem (34) associated with an edge $[v_0, v_1]$, can be rephrased as the minimization over the interval $[0, 1]$ of the smooth and convex function

$$f(t) := (1-t)l_0 + tl_1 + N_c((1-t)v_0 + tv_1).$$

Our first step is to numerically evaluate $f'(0) = l_1 - l_0 + \langle \nabla N_c(v_0), v_1 - v_0 \rangle$, and likewise $f'(1)$, see Remark 3.6 for the numerical computation of $\nabla N_c(v)$. If $f'(0) \geq 0$ (resp. $f'(1) \leq 0$), then the convex function f reaches its minimum at 0 (resp. at 1), and the problem is solved.

Otherwise, recall that the value to be computed reads

$$\min_{\xi \in \Xi_1} \langle l, \xi \rangle + N_c(V\xi) = \min_{\xi \in \Xi_1} \max_{N_c^*(p) \leq 1} \langle l, \xi \rangle + \langle p, V\xi \rangle.$$

Exchanging the min and max, and using the optimality relation (35, left), we rephrase (34) as

$$\max\{\lambda; (\lambda, p) \in \mathbb{R} \times \mathbb{R}^d,\ \lambda \mathbb{1}_1 = l + V^{\mathrm{T}} p,\ N_c^*(p) \leq 1\}. \tag{38}$$

This problem has the same structure as the primal norm $N_c(v)$ computation, see (25), up to the additional linear equality constraint which raises no particular issue. It is solved using the same approach, namely a reformulation of the contraint as (27, right), and SQCQP, see Appendix C (a.k.a. we repeatedly solve, in closed form, the approximate problem where the non-linear constraint is replaced with a second order expansion). For best efficiency, an initial guess for (λ, p) is constructed from the norm gradients at v_0 and v_1, and a quadratic model.

Face (k=2). We turn to the optimization problem (34), posed on a triangle of vertices (v_0, v_1, v_2). Our first step is to minimize (34) over the edges $[v_0, v_1]$, $[v_1, v_2]$, and $[v_2, v_0]$ as described in the previous paragraph. Examining the norm gradients at these minimizers, one can decide whether the minimum of the convex optimization problem (34) is attained on the boundary of Ξ, in which case the problem is solved.

Otherwise, since V is a square invertible matrix, we can invert (35, left) into $p = V^{-\mathrm{T}}(\lambda 1 - l)$, and turn (35, right) into an univariate polynomial equation of degree 2d w.r.t $\lambda \in \mathbb{R}$

$$\det(\mathrm{Id} - m_c(V^{-\mathrm{T}}(\lambda 1 - l))) = 0. \tag{39}$$

A Newton method is used to solve this equation, with a suitable initial guess based on the result of the minimization over the three edges $[v_0, v_1]$, $[v_1, v_2]$, $[v_2, v_0]$, and a quadratic model.

4 Numerical experiments

In this section, we present numerical experiments to illustrate the properties of the numerical solver introduced in this study. We first perform convergence order and computational complexity analysis. To do so, we make use of particular 3D metrics computed from the conformal transformation of constant metrics. This conformal transformation makes it possible to determine an analytical solution of the eikonal equation in a 3D anisotropic medium presenting heterogeneities (spatial variations of its elastic properties).

In a second experiment, we consider a 3D general anisotropic medium coming from the homogenization of the 3D SEG/EAGE overthrust benchmark model, which is widespread in the seismic exploration community. For this model, no analytical solution to the eikonal equations exist. Therefore, we validate our approach by comparing the first-arrival travel-time we compute with the wavefront of the 3D elastic wave equation solution computed in the same medium, using a volumetric method (spectral element strategy).

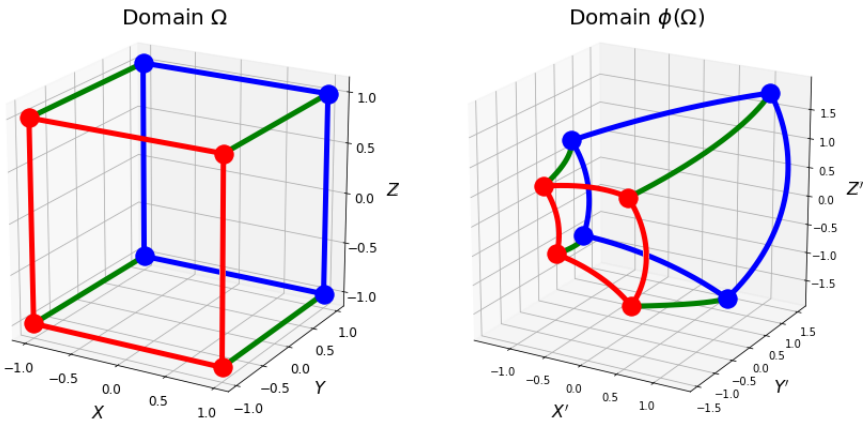

Figure 3: Edges of the domain $\widetilde{\Omega} =]-1,1[^3$ (a cube) and of its image $\Omega = \phi(\widetilde{\Omega})$ by the special conformal transformation (40). See §4.1 and §A.

These two experiments also illustrate the ubiquity and various causes of anisotropy in seismic data. Indeed the design of the first experiment involves Hooke tensors associated with crystals, whose anisotropy originates from the atomic layout at the nanometer scale [BC91]. In contrast, the second experiment illustrates the apparent anisotropy arising from homogeneization at the interfaces of kilometer wide structures [CMA+20]. Let us also acknowledge that a central assumption of homogeneization techniques is that the seismic waves have a limited frequency spectrum, in apparent contradiction with the eikonal equation formalism which is derived from the high frequency approximation; this point deserves investigation in its own right, both theoretical and numerical, but is outside of the scope of this paper.

4.1 Convergence order and computational complexity

In order to validate the convergence order of the proposed method, we generate a non-trivial test case with an explicit solution, obtained as the conformal transformation of a constant material. We refer to §A for details, and simply mention here that the test is parametrized by a (single) Hooke tensor c and a vector $b \in \mathbb{R}^3$, features a fully non-trivial metric on $\widetilde{\Omega} :=]-1,1[^3$, and admits the following explicit solution:

$$\tilde{u}(x) = N_c(\phi(x) - x^*), \qquad \text{with } \phi(x) := \frac{x - b\|x\|^2}{1 - 2\langle b, x\rangle + \|b\|^2\|x\|^2}. \tag{40}$$

For the numerical tests, we consider the Hooke tensors for both the olivine and mica media as defined in Table 1. The olivine medium has orthorhombic symmetry, and an anisotropic length distortion of approximately 0.265. The mica medium has hexagonal symmetry, and an anisotropic length distortion of approximately 0.753. We use our numerical scheme with three different 3D geometrical stencils (cut-cube, cube and spiky-cube), see Figure 1.

We have already shown in §2.3 that all three stencils give a causal scheme for the length distortion of the olivine. Indeed we can see in Figure 5 that the L^2-error decreases with the expected order (2 or 3) with the step size of the grid, whereas the computation time is proportional to the total number of grid points.

However, for the mica, only the spiky-cube stencil guarantees a causal scheme. As can be expected, we see in Figure 6 that the cut-cube and cube stencils give poor results here, with a

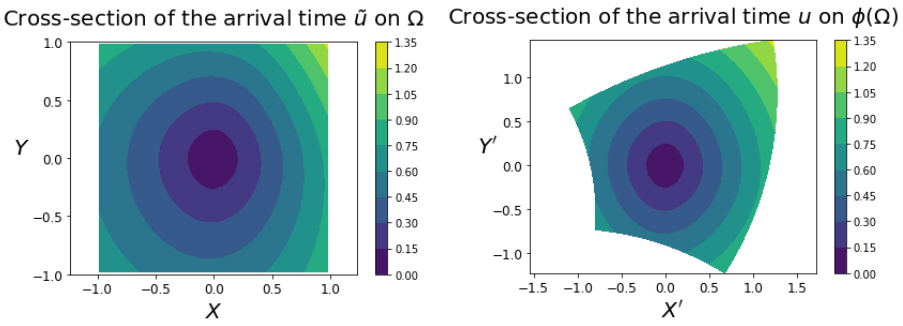

Figure 4: Cross-section at $Z = 0$ of the arrival time for a non-trivial metric on $\widetilde{\Omega}$ (left), which corresponds to a constant metric on the transformed domain $\Omega = \phi(\widetilde{\Omega})$ (right). See §4.1 and §A.

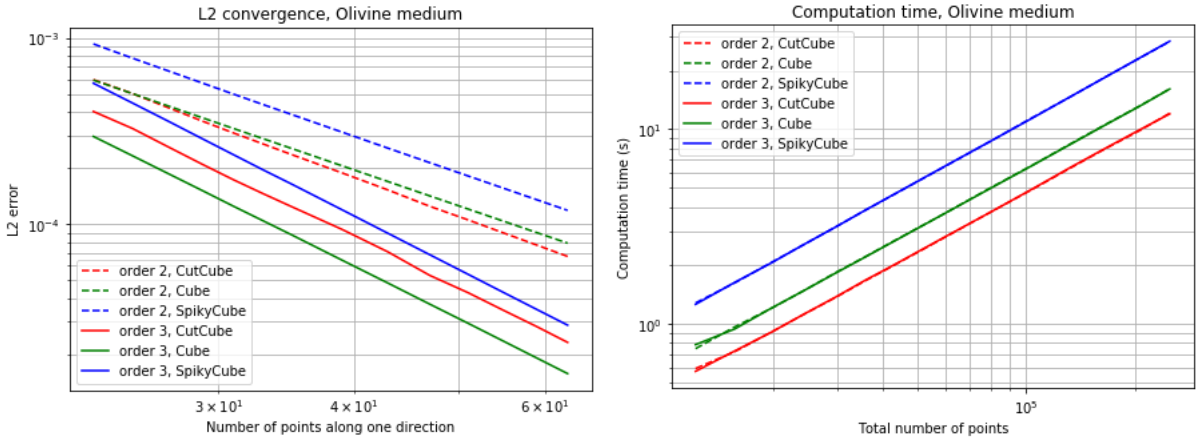

Figure 5: Convergence orders for the olivine, comparison between stencils

systematic error coming from the scheme being non causal. Conversely, the spiky-cube stencil provides the expected order of convergence. An alternative approach to ensure convergence, not illustrated here, would be to use the non-causal cut-cube or cube stencils in combination with an iterative solver such as the fast sweeping method.

Remark 4.1. *The complexity of the fast marching method is* $\mathcal{O}(C_0 N \ln N + C_1 N)$*, where the first term accounts for the cost of maintaining a priority queue of the non-accepted points, and the second term accounts for the numerical evaluation of the update operator* (8)*, see Lines 2. and 5. respectively in Algorithm 1 in §2.2. The structure of the norm involved in the update operator of this study is rather complex since it is defined implicitly, see Equation* (5)*, from an already complex algebraic expression, see Equation* (1)*. As a result one has* $C_1 \gg C_0$ *and the second contribution* $\mathcal{O}(C_1 N)$ *to the complexity is dominant in our numerical experiments (see Fig 5 and Fig 6), typically accounting for* 90% *of the CPU time.*

These numerical experiments on non-trivial 3D metrics confirm that our numerical solver achieves third order convergence and a quasi-linear computation time.

4.2 Numerical validation in a 3D fully anisotropic medium

We consider here a 3D model with a fully anisotropic Hooke tensor (21 independent coefficients). This model is obtained through the homogenization (equivalent medium theory) of a fine scale

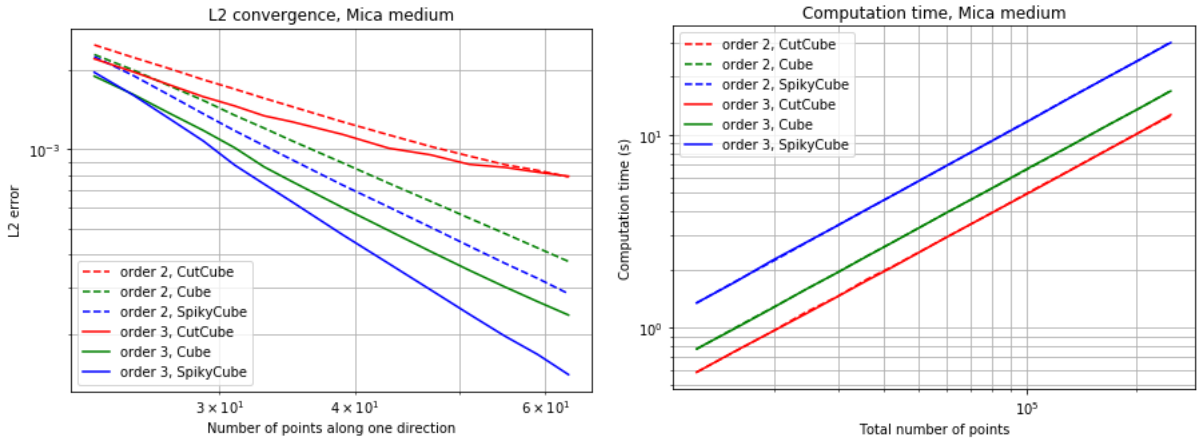

Figure 6: Convergence orders for the mica, comparison between stencils

isotropic model, known as the SEG/EAGE overthrust model.

The SEG/EAGE overthrust model is a 3D exploration scale benchmark subsurface model designed in the 1990s to foster the development of wave propagation modeling and inversion tools. It covers an area of 20 km $\times$ 20 km $\times$ 4 km. It represents an onshore structure affected by erosion, in which can be identified faults, a salt layer, and superficial lateral velocity variations induced by buried topography, channels and lenses. More details can be found in [ABK97].

The initial SEG/EAGE overthrust model is an isotropic model described by pressure and shear wave velocities, and density. Recently, as an illustration of non-periodic two-scale homogenization for elastic media, an upscaled version of the SEG/EAGE overthrust model has been presented [CMA$^+$20]. This branch of homogenization, derived from micro-mechanics [BLP78], aims at computing effective subsurface elastic models for seismic waves propagating at finite-frequency. The leading idea is that subsurface heterogeneities smaller than the propagated wavelengths lead to apparent anisotropy. Effective subsurface media for a given frequency range thus correspond to smooth fully anisotropic media. This theory has now been well established (see [CC18] and references therein). The interest is to reduce the computational cost for volumetric wave propagation method, the computation in a smooth anisotropic medium making it possible to use a coarse Cartesian grid instead of the fine unstructured mesh which would be required in the corresponding isotropic fine scale model. Homogenization starts also to be looked at for better constraining the solution space of seismic imaging problems [CM18].

In this study, we use the homogenized version of the 3D SEG/EAGE overthrust model presented in [CMA$^+$20], therefore a fully anisotropic medium with 21 independent coefficients, and a density model. These models are described on a Cartesian grid containing $534 \times 534 \times 107$ points. This makes it possible for us to access a realistic and physically meaningful fully anisotropic stiffness tensor. To assess and illustrate the accuracy of our Fast Marching based eikonal solver, we compare the first-arrival travel-times we compute with a 3D wavefront propagating from a source located in the middle of the medium at the surface at $x = 10$ km, $y = 10$ km, $z = 0$ km.

The 3D wave propagation problem is solved using the spectral-element based modeling and inversion code SEM46 [TBM$^+$19, CBM20]. The simulation is performed using a 10 Hz Ricker vertical force source, on a Cartesian-based mesh using 560 $\times$ 560 $\times$ 110 elements with P^4 Lagrange polynomial. The final time for simulation is set to 2.5 s leading to 10000 time steps

with a time sampling $\Delta t = 0.00025$ s. The computation has been performed on the Univ. Grenoble Alpes HPC Dahu platform on 6 nodes of 32 cores (192 cores in total) benefiting from the domain-decomposition algorithm implemented in SEM46. Each node is equipped with two xeon Skylake Gold Intel processors, each featuring 16 cores clocked at 2.1 GHz, and 192 GO of RAM. The elapsed time for the computation in such settings is approximately 3.5 hours.

For the eikonal solver, the anisotropic length distortion is sufficiently small so that the cut-cube stencil is causal. Compared to the full wave modeling using SEM46, the computation of the eikonal solution on the $534 \times 534 \times 107$ grid on a single core of a laptop (with Intel architecture comparable to the one from the Univ. Grenoble Alpes cluster) took approximately 1600s (less than half an hour).

We present in Figure 7 a 3D view of the superposition of the isochrones for the first-arrival travel time computed through our eikonal solver with the wavefront computed using SEM46, at time $t = 1.5$ s, $t = 2$ s, and $t = 2.5$ s. The P-wave velocity model appears in the background. As can be seen, the isochrone contours (in red) accurately follow the elastic wavefront (in black and white) for the different snapshots. Noticeable irregularities of the wavefront can be identified close to the fastest variations of the P-wave velocity model, which are reproduced accordingly using our eikonal solver. Of course, due to finite-frequency effect of the 3D wave propagation problem, the correspondence is not expected to be perfect, however the qualitative match we observe is a validation of our approach on a realistic 3D example.

We complete this comparison with the presentation of a seismogram in Figure 8. The seismogram is extracted on a receiver line at the surface, in the place of the source, from x=0 to $x = 20$ km. On this seismogram, we superpose the first-arrival travel-time computed through our eikonal solver. Again, we can identify a qualitative match between our eikonal solver solution and the first-break of the synthetic seismogram extracted from the wave propagation simulation.

5 Conclusion

We presented a numerical solver for the 3D eikonal equation with anisotropy coming from a general Hooke tensor. It uses a single pass method similar to the fast marching method and features a source factorization, which leads to a quasi-linear complexity and up to third-order accuracy.

The scheme features one parameter, which is the choice of discretization stencil, see Figure 1. For the overwhelming majority of materials encountered in seismology, the compact cut-cube stencil provides best results in terms of both accuracy and computation time. However if strongly anisotropic crystalline materials are considered, such as mica, and if one insists in using the single pass fast marching method (as opposed to e.g. the fast sweeping iterative method) to solve the discretized PDE, then a somewhat wider stencil is needed to ensure consistency.

Future research will be devoted to (i) applications to seismic imaging by tomographic inversion, (ii) extensions of the method (to take into account the topography, multiple arrivals, amplitude effects, ...), and (iii) optimizations of the scheme for special classes of Hooke tensors such as tilted transversly isotropic materials.

Code availability. A software library which implements the numerical method presented in this study can be found at: `https://github.com/Mirebeau`.

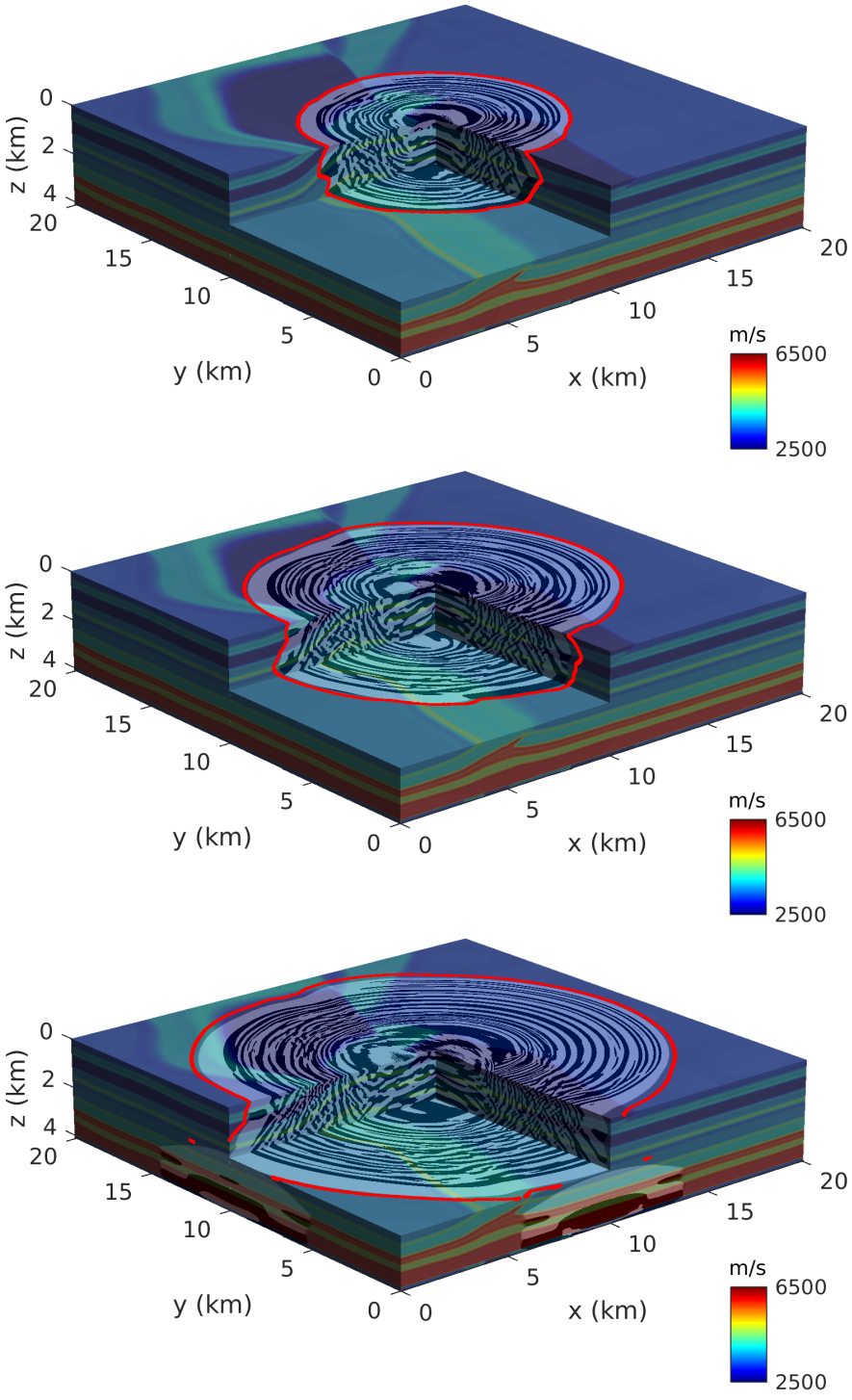

Figure 7: Elastic wavefield (black and white) computed in the 3D fully anisotropic medium coming from the homogenization of the SEG/EAGE overthrust model. The background corresponds to $\sqrt{\frac{C_{33}}{\rho}}$, that is the P-wave velocity of this model if it had a VTI symmetry (which is not the case, but it is still a good approximation for illustrative purposes). The red contour corresponds to the isochrone computing through our Fast Marching eikonal solver. The different snapshots are obtained at $t = 1.5$ s (top), $t = 2$ s (middle) and $t = 2.5$ s (bottom).

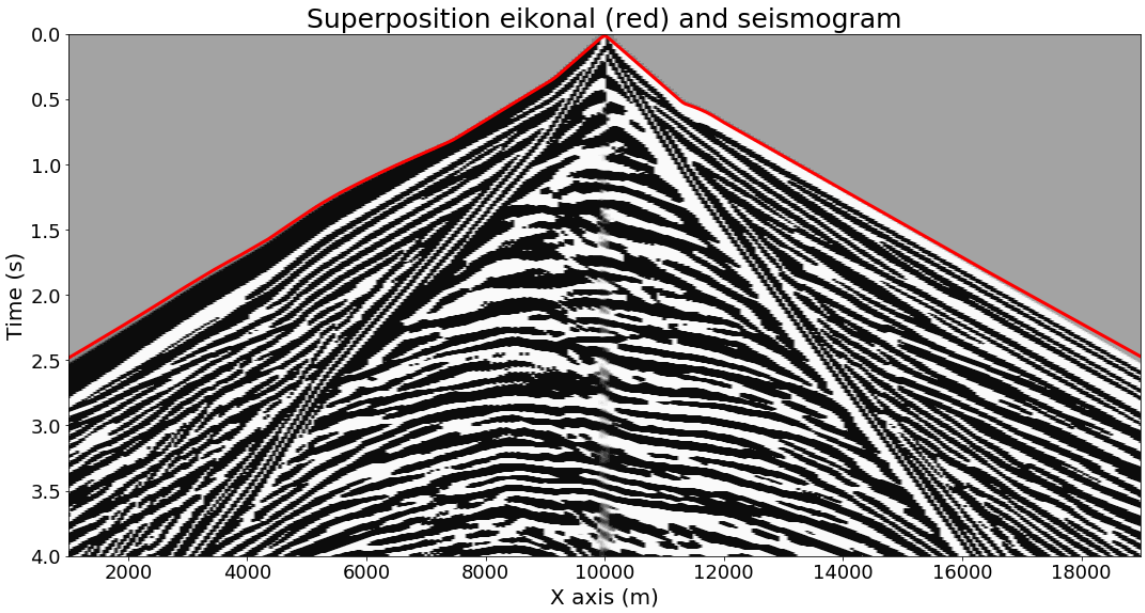

Figure 8: Seismogram recorded along a receiver line located on the surface ($z = 0$ km), in the source plane ($y = 10$ km) along the x-axis (from $x = 0$ km to $x = 20$ km). The vertical displacement is recorded. The vertical displacement intensity is represented in black and white. The first-arrival travel-time computing through our eikonal solver for each receiver position is superposed to the seismogram in red. The resulting red-contour matches the synthetic first-arrival travel-time corresponding to the 3D spectral-element simulation.

Acknowledgements This study was partially funded by the SEISCOPE consortium (*http://seiscope2.osug.fr*), sponsored by AKERBP, CGG, CHEVRON, EQUINOR, EXXON-MOBIL, JGI, SHELL, SINOPEC, SISPROBE and TOTAL. This study was granted access to the HPC resources of the Dahu platform of the CIMENT infrastructure (*https://ciment.ujf-grenoble.fr*), which is supported by the Rhône-Alpes region (GRANT CPER07_13 CIRA), the OSUG@2020 labex (reference ANR10 LABX56) and the Equip@Meso project (reference ANR-10-EQPX-29-01) of the programme Investissements d'Avenir supervised by the Agence Nationale pour la Recherche, and the HPC resources of CINES/IDRIS/TGCC under the allocation 046091 made by GENCI.

This research has received funding from the European Union's Horizon 2020 research and innovation programme under the ENERXICO project, grant agreement No. 828947.

Hugo Leclerc helped with the optimization of the numerical implementation of a critical subroutine, which accounts for the bulk of the computation time of our numerical method, namely the evaluation of $\det(\mathrm{Id} - m_c(v))$ and of its gradient and hessian (27).

A Construction of the synthetic test

We describe the synthetic test used §4.1 to validate the convergence order of the proposed numerical scheme. For that purpose, we need to introduce some notations.

Definition A.1. *Let $\Omega \subset \mathbb{R}^d$ be a domain, equipped with a metric $N_x(v)$ (resp. dual-metric $N_x^*(p)$), $x \in \Omega$, $p, v \in \mathbb{R}^d$. Their pull-back by a diffeomorphism $\phi : \widetilde{\Omega} \to \Omega$, whose Jacobian matrix is denoted Φ, is defined as*

$$\widetilde{N}_x(v) := N_{\phi(x)}\big(\Phi(x)v\big), \qquad \Big(\textit{resp. } \widetilde{N}_x^*(p) := N_{\phi(x)}^*\big(\Phi^{-T}(x)p\big).\Big)$$

By construction, the geometrical quantities defined §2.1 and associated with the metrics N_x and $\widetilde{N}_x$ are closely related: the path-length $\widetilde{\mathcal{L}}(\gamma) = \mathcal{L}(\gamma \circ \phi)$, and distance $\tilde{d}(x, y) = d(\phi(x), \phi(y))$, where $x, y \in \widetilde{\Omega}$ and $\gamma : [0, 1] \to \Omega$. Likewise, if $u : \Omega \to \mathbb{R}$ obeys the eikonal equation (2), then so does $u \circ \phi : \widetilde{\Omega} \to \mathbb{R}$ w.r.t. the pulled-back dual-metric $\widetilde{N}_x^*$, with the appropriate seed point and boundary conditions. In our experiments, we use for simplicity a metric $N_x = N_c$ defined by a constant field of Hooke tensors c, and a star-shaped domain Ω w.r.t. the origin, which is chosen as the seed point; the eikonal equation on Ω (resp. $\widetilde{\Omega}$) therefore admits the following explicit solution, as announced in (40):

$$u(x) = N_c(x), \qquad \Big(\text{resp. } \tilde{u}(x) = N_c\big(\phi(x)\big).\Big)$$

In general, the pull-back of a metric defined by a Hooke tensor is *not* defined by a Hooke tensor alone, and one has in addition to keep track of the Jacobian matrix both symbolically and numerically. A special case of interest arises however for *conformal transformations*, whose Jacobian is a scaled rotation, and which thus preserve the metric structure. More precisely, let $x \in \widetilde{\Omega}$ be fixed, assume that $N_{\phi(x)}^*$ is defined as in (1) by a Hooke tensor c, and that $\Phi(x) = \lambda R$ is the product of a scaling $\lambda > 0$ and of a rotation R. Then $\widetilde{N}_x^*$ is defined by the Hooke tensor of components

$$\tilde{c}_{i'j'k'l'} = \lambda^{-2} \sum_{i,j,k,l} c_{ijkl} R_{ii'} R_{jj'} R_{kk'} R_{ll'}.$$

Another benefit of conformal transformations is that they leave invariant the length distortion and angular width of the metric, $\mu(\widetilde{N}_x) = \mu(N_{\phi(x)})$ and $\mu(\widetilde{N}_x) = \mu(N_{\phi(x)})$, see Definitions 2.2

and 2.4. Three dimensional conformal transformations include dilations, translations, rotations, the inversion $x \in \mathbb{R}^3 \setminus \{0\} \mapsto x/\|x\|^2$, and compositions of these.

In our experiments we use a "special conformal transformation", see (40, right) and Figure 3, which is smooth except for a singularity at $b/\|b\|^2$, where $b \in \mathbb{R}^3$ is a parameter. It is obtained as the composition of an inversion, a translation by $-b$, and another inversion. More precisely, we choose $b = (1/6, 1/9, 1/18)$ and let $\widetilde{\Omega} :=]-1, 1[^3$ with seed at the origin, so that the singular point $b/\|b\|^2 \notin \widetilde{\Omega}$, and the image domain $\Omega := \phi(\widetilde{\Omega})$ is star shaped w.r.t. the origin, see Figure 3. Besides, we use the Hooke tensors of the olivine and mica as defined in Table 1, with a constant rotation of Euler axis $(2, 1, 3)$ and angle $3\pi/5$.

B Proof of proposition 2.6

We estimate in this appendix the quantity $\Theta(N)$, which measures the angular distortion associated with a norm N on $\mathbb{R}^d$, in terms of its length distortion, as announced in Proposition 2.6. Different proof techniques are used in the elliptic and anelliptic cases.

B.1 Anelliptic norms

The announced estimate, established in Corollary B.2, follows from upper and lower bounds on the gradient of a norm, presented in the next lemma.

Lemma B.1. *Let N be a norm on $\mathbb{R}^d$, differentiable at $v \in \mathbb{R}^d \setminus \{0\}$. Then*

$$\mu_*(N) \leq \|\nabla N(v)\| \leq \mu^*(N).$$

Proof. Since N is 1-homogeneous, one has $\langle \nabla N(v), v \rangle = N(v)$ by Euler's identity, and therefore

$$\mu_*(N) \leq \frac{N(v)}{\|v\|} = \frac{\langle \nabla N(v), v \rangle}{\|v\|} \leq \|\nabla N(v)\|.$$

On the other hand, for any vector w one obtains using successively the convexity of N and the triangular inequality

$$\langle \nabla N(v), w \rangle \leq N(v + w) - N(v) \leq N(w).$$

Choosing $w := \nabla N(v)$ yields the announced upper estimate and concludes the proof:

$$\mu^*(N) \geq \frac{N(\nabla N(v))}{\|\nabla N(v)\|} \geq \frac{\langle \nabla N(v), \nabla N(v) \rangle}{\|\nabla N(v)\|} = \|\nabla N(v)\|. \qquad \square$$

Corollary B.2. *For any norm N on $\mathbb{R}^d$, differentiable on $\mathbb{R}^d \setminus \{0\}$, one has $\mu(N) \cos \Theta(N) \geq 1$.*

Proof. Using Lemma B.1 we obtain as announced

$$\cos \Theta(N) = \frac{\langle v, \nabla N(v) \rangle}{\|v\| \|\nabla N(v)\|} = \frac{N(v)}{\|v\|} \frac{1}{\|\nabla N(v)\|} \geq \mu_*(N)/\mu^*(N) = 1/\mu(N). \qquad \square$$

B.2 Elliptic norms

The announced estimate, established in Corollary B.4, follows from a classical inequality in analysis, whose proof is recalled in the next lemma.

Lemma B.3 (Weighted Pólya-Szegö inequality)**.** *Let $(\lambda_i)_{i=1}^d$ be positive numbers, and $(\mu_i)_{i=1}^d$ be non-negative, let $\lambda_* = \min\{\lambda_1, \cdots, \lambda_d\}$ and let $\lambda^* := \max\{\lambda_1, \cdots, \lambda_d\}$. Then*

$$\sqrt{\sum_{1\leq i\leq d} \mu_i\lambda_i}\sqrt{\sum_{1\leq i\leq d} \frac{\mu_i}{\lambda_i}} \leq \frac{1}{2}\left(\sqrt{\frac{\lambda^*}{\lambda_*}} + \sqrt{\frac{\lambda_*}{\lambda^*}}\right)\sum_{1\leq i\leq d} \mu_i.$$

Proof. W.l.o.g we may assume that $\sum_{1\leq i\leq d}\mu_i = 1$, and denote $E[\gamma] := \sum_{1\leq i\leq d}\mu_i\gamma_i$ for any sequence $(\gamma_i)_{i=1}^d$. Observing that $E[(\lambda^* - \lambda)(1/\lambda_* - 1/\lambda)] \geq 0$, and developping, we obtain

$$\frac{\lambda^*}{\lambda_*} + 1 \geq E\left[\frac{\lambda^*}{\lambda}\right] + E\left[\frac{\lambda}{\lambda_*}\right] \geq 2\sqrt{E\left[\frac{\lambda^*}{\lambda}\right]E\left[\frac{\lambda}{\lambda_*}\right]}.$$

The second inequality follows from the of the arithmetic-geometric mean inequality $\frac{a+b}{2} \geq \sqrt{ab}$, $\forall a, b \geq 0$. The announced result follows. □

Corollary B.4. *For any elliptic norm N one has $\frac{1}{2}(\mu(N) + \mu(N)^{-1})\cos\Theta(N) = 1$.*

Proof. Without loss of generality, up to a rotation, we may assume that for all $v \in \mathbb{R}^d$

$$N(v)^2 = \sum_{1\leq i\leq d} \lambda_i v_i^2, \qquad \text{thus} \quad N(v)\nabla N(v) = (\lambda_i v_i)_{i=1}^d,$$

where $\lambda_1, \cdots, \lambda_d > 0$. Denote $\lambda_* = \min\{\lambda_1, \cdots, \lambda_d\}$ and $\lambda_* = \max\{\lambda_1, \cdots, \lambda_d\}$, so that $\mu(N) = \sqrt{\lambda^*/\lambda_*}$. Then letting $\mu_i := \lambda_i v_i^2$ one obtains by Lemma B.3

$$\frac{\|\nabla N(v)\|\|v\|}{\langle \nabla N(v), v\rangle} = \frac{\sqrt{\sum_i \lambda_i^2 v_i^2}\sqrt{\sum_i v_i^2}}{\sum_i \lambda_i v_i^2} = \frac{\sqrt{\sum_i \mu_i\lambda_i}\sqrt{\sum_i \mu_i/\lambda_i}}{\sum_i \mu_i} \leq \frac{1}{2}\left(\sqrt{\frac{\lambda^*}{\lambda_*}} + \sqrt{\frac{\lambda_*}{\lambda^*}}\right). \tag{41}$$

This proves $\frac{1}{2}(\mu(N) + \mu(N)^{-1})\cos\Theta(N) \geq 1$. Adequately choosing v turns (41) into an equality, which concludes the proof. More precisely, we may assume w.l.o.g that $\lambda_* = \lambda_1$ and $\lambda^* = \lambda_2$, and then choose $v = (\sqrt{\lambda_2}, \sqrt{\lambda_1}, 0, \cdots, 0)$. □

C Sequential quadratically constrained programming

The numerical implementation of our eikonal equation solver involves the solution to optimization problems of the form

$$\max\{\langle p, v\rangle;\ f(p) \leq 0\}, \tag{42}$$

where f is smooth and strongly convex, and the vector v is fixed. They arise in the definition of the norm (25), which is used in the source factorization (20), as well as in evaluation of the update operator on vertices and edges (38), with an additional linear constraint in the latter case. In order to solve (42), we use an approach known as Sequential Quadratically Constrained Quadratic Programming (SQCQP) [FLT03], whose basic principle is to solve a sequence of simplified problems obtained by replacing the objective function and the constraints with their second order Taylor expansion. We provide two basic results that are sufficient for our application, and refer to [FLT03] for more details on this rich theory. Our first observation, whose proof is left to the reader, is that the problem (42) has a closed form solution when f is a suitable quadratic function.

Lemma C.1 (Maximization of a linear function over an ellipsoid)**.** *Let $f : \mathbb{R}^d \to \mathbb{R}$ be a quadratic function such that the set $\{f < 0\}$ is a non-empty ellipsoid, and let $p, v \in \mathbb{R}^d$. Then*

$$F(p) := p + M(p)(\lambda(p)v - V(p)) \tag{43}$$

is the unique solution to (42)*, where*

$$V(p) := \nabla f(p), \qquad M(p) := (\nabla^2 f(p))^{-1}, \qquad \lambda(p) := \sqrt{\frac{\langle V(p), M(p)V(p)\rangle - 2f(p)}{\langle v, M(p)v\rangle}}. \tag{44}$$

For convenience, the solution (43) is expressed in terms of the Taylor expansion of the quadratic function f at a given but arbitrary point p. Note however that, if f is a quadratic function as assumed in Lemma C.1, then the matrix $M(p)$ in (44, center) is independent of p, and the value of $F(p)$ is independent of p since it solves (42). The basic SQCQP framework consists in repeatedly evaluating (43) with a *non-quadratic* function f, thus generating a sequence of points $p_{n+1} = F(p_n)$, $n \geq 0$. This yields an iterative method for the optimization problem (42), enjoying a quadratic (Newton-like) local convergence rate, as shown in Proposition C.2. Variants of this method enjoy a global convergence guarantee [FLT03] under suitable assumptions, but in our numerical experiments the basic method was adequate.

Proposition C.2. *Let $f : \mathbb{R}^d \to \mathbb{R}$ be C^3 smooth, and let $v \in \mathbb{R}^d$. Assume that $p_* \in \mathbb{R}^d$ and $\lambda_* > 0$ are such that*

$$f(p_*) = 0 \qquad \nabla f(p_*) = \lambda_* v \qquad \nabla^2 f(p_*) \succ 0. \tag{45}$$

Then p_* is an isolated local maximum for the optimization problem (42)*. In addition there exists a constant $C > 0$ such that, for any $p_0 \in \mathbb{R}^d$ close enough to p_*, the sequence defined by $p_{n+1} = F(p_n)$, see* (43)*, satisfies for all $n \geq 0$*

$$\|p_n - p_*\| \leq C^{-1}(C\|p_0 - p_*\|)^{2^n}. \tag{46}$$

Sketch of proof. We recognize in (45) the second-order optimality conditions for the constrained optimization problem (42). A first order Taylor expansion shows that $\lambda(p_* + h) = \lambda_* + \mathcal{O}(h^2)$, and then $F(p_* + h) = p_* + \mathcal{O}(h^2)$. The estimate (46) follows by induction on $n \geq 0$. □

Remark C.3 (Exponential transformation, and numerical stability)**.** *Assume that the constraint in* (42) *takes the form $g \leq 0$, where $g = \exp(\alpha f) - 1$ is a strongly convex function, defined in terms of a smooth (but non-convex) f and a positive constant α. One can check that $(g, \nabla g, \nabla^2 g)$ is positively proportional to*

$$\tilde{f} := (1 - \exp(-\alpha f))/\alpha, \qquad \nabla f, \qquad \nabla^2 f + \alpha \nabla f \nabla f^T.$$

Note also that f and $\tilde{f}$ vanish at the same points, and if p_* is such a point then $\tilde{f}(p_* + h) = f(p_* + h) + \mathcal{O}(\|h\|^2)$ for small h. In the sequential quadratic iterations, see Proposition C.2, one may thus replace $(g, \nabla g, \nabla^2 g)$ with $(f, \nabla f, \nabla^2 f + \alpha \nabla f \nabla f^T)$ and preserve the local quadratic convergence (46)*. This eliminates all exponentials, to the benefit of numerical stability.*

D Monotony and causality in fixed point problems

In this section, we review the properties of the numerical scheme considered in this paper, and derive the following guarantees: existence and uniqueness of a fixed point, convergence of an iterative method to find it, and validity of the fast-marching method subject to an acuteness condition. We also discuss how these properties transfer to the source factored and high order scheme variants. Closely related arguments can be found in the literature devoted to semi-Lagrangian discretizations of the eikonal equation [Tsi95, SV01, AM12, BR06, Mir14b, Mir14a]. We fix the grid scale $h > 0$ in this appendix, and refer to [BR06] for a convergence analysis to the PDE solution as it is refined. Denote $X := \Omega_h \setminus \{x_*\}$ the discretization set (4) minus the source point, and let $\mathbb{U} := \mathbb{R}^X$ be the set of mappings from X to $\mathbb{R}$. Recall that the objective is to find $u \in \mathbb{U}$ such that for all $x \in X$

$$\Lambda u(x) = u(x), \qquad \text{where } \Lambda u(x) := \min_{y \in \partial \mathcal{V}_h^x} \mathcal{I}_h^x u(y) + N_x(x-y), \tag{47}$$

where $\mathcal{I}_h^x$ denotes the piecewise linear interpolation operator, on a polytope $\mathcal{V}_h^x$ enclosing x, whose vertices lie on the grid $h\mathbb{Z}^d$, see §2.2. By convention in (47, right), $u \in \mathbb{U}$ is extended to $h\mathbb{Z}^d \setminus X$ by $u(x_*) = 0$ and $u = +\infty$ elsewhere. We make the following connectedness assumption: for any $x_0 \in X$, one can find $n \geq 1$ and $x_1, \cdots, x_n \in X$, such that x_{i+1} is a vertex of $\mathcal{V}_h^{x_i}$, for all $i < n$, and x_* is a vertex of $\mathcal{V}_h^{x_n}$. Given $u, v \in \mathbb{U}$, the strict inequality "$u < v$" stands for "$\forall x \in X, u(x) < v(x)$"; and likewise for weak inequality $u \leq v$. Given $u \in \mathbb{U}$ and $\tau \in \mathbb{R}$ we define

$$u^{\leq \tau}(x) := \begin{cases} u(x) & \text{if } u(x) \leq \tau, \\ +\infty & \text{else.} \end{cases}$$

Proposition D.1. *The operator $\Lambda : \mathbb{U} \to \mathbb{U}$ defined by (47, right) is continuous and obeys the following properties, where δ_0, δ_1 are positive constants, and where $u, v \in \mathbb{U}$, and $s, t \geq 0$, $\tau \in \mathbb{R}$ are arbitrary*

- *Monotone: if $u \leq v$ then $\Lambda u \leq \Lambda v$.*
- *Subadditive: $\Lambda(u + t) \leq \Lambda u + t$.*
- *δ_0-submultiplicative: $\Lambda[(1 + s)u] \leq (1 + s)\Lambda u - \delta_0 s$.*
- *Existence of a super-solution: there is $\underline{u} \in \mathbb{U}$ such that $\Lambda \underline{u} \leq \underline{u}$.*

If in addition $\Theta(N_x, \mathcal{V}_h^x) < \pi/2$ for all $x \in X$, then the operator Λ is also

- *δ_1-causal: if $u^{\leq \tau} = v^{\leq \tau}$ then $(\Lambda u)^{\leq \tau + \delta_1} = (\Lambda v)^{\leq \tau + \delta_1}$.*

Proof. The monotony of Λ follows from the monotony of linear interpolation $\mathcal{I}_h^x$. Likewise, the subadditivitity of Λ follows from the same property of $\mathcal{I}_h^x$ (actually $\Lambda(u + t) = \Lambda u + t$ at all points $x \in X$ whose stencil $\mathcal{V}_h^x$ does not contain the source x_*). Submutiplicativity is established as follows, using the 1-homogeneity of the interpolation operator $\mathcal{I}_h^x$

$$\min_{y \in \partial \mathcal{V}_h^x} (1 + s)\, \mathcal{I}_h^x u(y) + N_x(x-y) \leq (1 + s) \Big[\min_{y \in \partial \mathcal{V}_h^x} \mathcal{I}_h^x u(y) + N_x(x-y) \Big] - s \min_{y \in \partial \mathcal{V}_h^x} N_x(x-y),$$

thus with $\delta_0 = \min\{N_x(x-y);\, x \in X,\, y \in \partial \mathcal{V}_h^x\}$. Consider the *directed graph*, with an edge (x, y) of length $N_x(x-y)$ whenever y is a vertex of $\mathcal{V}_h^x$. Then the distance from a given point $x_0 \in X$ to the source x_*, denoted $\underline{u}(x_0)$, is finite by assumption and obeys $\Lambda \underline{u} \leq \underline{u}$. Finally, Proposition 2.3 establishes δ_1-causality with δ_1 the minimal value of $\|y - x\| \mu_*(N_x) \cos \Theta(N_x, \mathcal{V}_h^x)$ among all $x \in X$ and all vertices y of the stencil $\mathcal{V}_h^x$. □

In the rest of this appendix, we do not use the specific form (47, right) of the operator Λ, but only the properties established in Proposition D.1. From monotony, subadditivity, and δ_0-submultiplicativity, one derives the discrete comparison principle.

Proposition D.2 (Discrete comparison principle)**.** *Let $u, v \in \mathbb{U}$. If $u \leq \Lambda u$ and $\Lambda v \leq v$ then $u \leq v$. In addition, if either inequality is strict then $u < v$.*

Proof. Let $x \in X$ be such that $t := u(x) - v(x)$ is maximal, so that $u \leq v + t$ and $u(x) = v(x) + t$. Assuming that $t \geq 0$ we obtain $u(x) \leq \Lambda u(x) \leq \Lambda[v + t](x) \leq \Lambda v(x) + t \leq v(x) + t = u(x)$, by monotony and subadditivity. If either the first or last inequality is strict, we obtain a contradiction, thus $t < 0$ and therefore $u < v$ as announced. Otherwise note that $v_\varepsilon := (1 + \varepsilon)v$ obeys $v_\varepsilon < \Lambda v_\varepsilon$ for any $\varepsilon > 0$ by δ_0-submultiplicativity, thus $u < v_\varepsilon$ by the previous argument, hence $u \leq v$ by letting $\varepsilon \to 0$, which concludes the proof. □

Using in addition the continuity of Λ and the existence of a supersolution, one establishes that the fixed point problem (47, left) can be solved by iterating the operator. Finitely many iterations are sufficient if the operator is δ_1-causal.

Proposition D.3 (Convergence of the global iterative method)**.** *The operator Λ admits a unique fixed point $\boldsymbol{u}$, and for any $u \in \mathbb{U}$ one has $\Lambda^n u \to \boldsymbol{u}$ as $n \to \infty$. If in addition Λ is δ_1-causal and $u > 0$, then $\Lambda^n u = \boldsymbol{u}$ for all $n \geq \max(\boldsymbol{u})/\delta_1$.*

Proof. Proposition D.2 yields the uniqueness (but not the existence) of the fixed point $\boldsymbol{u}$. The null function $\overline{u} = 0$ satisfies $\Lambda\overline{u} \geq \delta_0 \geq 0 = \overline{u}$, by δ_0-submultiplicativity. Choose $t \geq 0$ sufficiently large so that $\overline{v} := \overline{u} - t \leq u \leq \underline{u} + t =: \underline{v}$, and note that $\overline{v} \leq \Lambda\overline{v}$ and $\Lambda\underline{v} \leq \underline{v}$ by subadditivity of Λ. Thus $\overline{v} \leq \cdots \leq \Lambda^n\overline{v} \leq \Lambda^n u \leq \Lambda^n\underline{v} \leq \cdots \leq \underline{v}$ by monotonicity of Λ, and induction on $n \geq 0$. By the monotone convergence theorem, $\Lambda^n\overline{v}$ and $\Lambda^n\underline{v}$ admit limits as $n \to \infty$. By continuity, these limits are fixed points of Λ, thus are equal to $\boldsymbol{u}$ by uniqueness. By the squeeze theorem we obtain $\Lambda^n u \to \boldsymbol{u}$ as announced.

Finally, assume that Λ is δ_1-causal, that $u > 0$, and note that $\boldsymbol{u} \geq \Lambda\overline{u} \geq \delta_0 > 0$. Then $u^{\leq 0} = \boldsymbol{u}^{\leq 0}$, and thus by induction $(\Lambda^n u)^{\leq n\delta_1} = (\Lambda^n \boldsymbol{u})^{\leq n\delta_1} = \boldsymbol{u}^{\leq n\delta_1}$ for all $n \geq 0$. The result follows. □

Global iteration is a poor way to allocate computational ressources in front propagation problems, and more efficient algorithms concentrate their efforts on a narrow band along the front. The convergence of iterative methods such as fast sweeping [QZZ07], the AGSI [BR06], or the FIM [JW08], follows from closely related arguments. The fast marching method Algorithm 1 [Tsi95] solves the fixed point problem (47, left) in finitely many steps with complexity $\mathcal{O}(N \ln N)$, see [Mir19, Proposition A.2] for a proof based on the properties established in Proposition D.1, causality included. We next establish that the properties of Proposition D.1 are stable under perturbation.

Proposition D.4 (Operator perturbation)**.** *Let $\alpha_*, \alpha^* \geq 0$, and for all $x \in X$ let $\alpha_x : X \to [-\alpha_*, \alpha^*]$. Define $\tilde{\Lambda} : \mathbb{U} \to \mathbb{U}$ by $\tilde{\Lambda}u(x) := \Lambda[u + \alpha_x](x)$. Then $\tilde{\Lambda}$ is continuous, monotone, subadditive, is $(\delta_0 - \alpha^*)$-submultiplicative if $\delta_0 > \alpha_*$, and admits the super-solution $(1 + \alpha^*/\delta_0)\underline{u}$. If Λ is δ_1-causal with $\delta_1 > \alpha_*$, then $\tilde{\Lambda}$ is $(\delta_1 - \alpha_*)$-causal.*

Proof. Fix $x \in X$, $u, v \in \mathbb{U}$, and $s, t \geq 0$. The continuity of $\tilde{\Lambda}$ immediately follows from the continuity of Λ. If $u \leq v$, then $u + \alpha_x \leq v + \alpha_x$, thus $\Lambda[u + \alpha_x] \leq \Lambda[v + \alpha_x]$ since Λ is monotone, therefore $\tilde{\Lambda}$ is monotone. One has $\Lambda[u + t + \alpha_x] \leq \Lambda[u + \alpha_x] + t$ by subadditivity of Λ, thus $\tilde{\Lambda}$ is subadditive. One has $\Lambda[(1 + s)u + \alpha_x] = \Lambda[(1 + s)(u + \alpha_x) - s\alpha_x] \leq \Lambda[(1 + s)(u + \alpha_x) + s\alpha_*] \leq$

$\Lambda[(1+s)(u+\alpha_x)] + s\alpha_* \leq (1+s)\Lambda[u+\alpha_x] - \delta_0 s + s\alpha_*$, using successively the monotony, subadditivity, and δ_0-submultiplicativity of Λ, thus $\tilde{\Lambda}$ is $(\delta_0 - \alpha_*)$-submultiplicative if $\delta_0 > \alpha_*$. One has $\Lambda[(1+s)\underline{u} + \alpha_x] \leq \Lambda[(1+s)\underline{u}] + \alpha^* \leq (1+s)\Lambda\underline{u} - \delta_0 s + \alpha^*$, by subadditivity and submultiplicativity of Λ, thus choosing $s = \alpha^*/\delta_0$ yields a supersolution of $\tilde{\Lambda}$. Finally, if Λ is δ_1-causal and $u^{\leq\tau} = v^{\leq\tau}$, then $(u+\alpha_x)^{\leq\tau-\alpha_*} = (v+\alpha_x)^{\leq\tau-\alpha_*}$ and therefore $(\Lambda[u+\alpha_x])^{\leq\tau-\alpha_*+\delta_1} \leq (\Lambda[v+\alpha_x])^{\leq\tau-\alpha_*+\delta_1}$, thus $\tilde{\Lambda}$ is $(\delta_1 - \alpha_*)$-causal. □

The *first order source factorization* (21) falls in the framework of Proposition D.4, with $\alpha_x(y) := u_*(x) - u_*(y) + \langle \nabla u_*(x), y - x\rangle$, which satisfies $\alpha_x(y) = \mathcal{O}(h^2/\|x - x_*\|)$, where u_* is the source factor and x_* is the source point. On the other hand, inspection of the proof of Proposition D.1 yields that $\delta_0 = \hat{\delta}_0 h$ and $\delta_1 = \hat{\delta}_1 h$ where $\hat{\delta}_0$ and $\hat{\delta}_1$ are independent of the grid scale h. Thus $\delta_0 \geq \|\alpha_x\|_\infty$ and $\delta_1 \geq \|\alpha_x\|_\infty$ when h is sufficiently small (except for points x in a ball of radius $\mathcal{O}(h)$ around the source point x_*), and thus Proposition D.4 applies to the factored scheme.

The *second and third order schemes* define perturbations (22) and (23) which depend on the unknown u, and thus do *not* fall in the framework of Proposition D.4. That is the reason why, following [Set99], we use them in a cautious way: only in the post-processing step of the fast marching method right before the accepted value is frozen[4] see line 3 of Algorithm 1, and only if their magnitude does not exceed Ch^2 where C is an absolute constant. Together, these limitations ensure that the fast marching algorithm still terminates in a single pass over the domain, and produces an output obeying $\Lambda u = u + \mathcal{O}(h^2)$. Therefore $u = \boldsymbol{u} + \mathcal{O}(h)$ where $\boldsymbol{u}$ is the solution of the original scheme, by Proposition D.5 below. In other words, we cannot prove that the high order variants of the scheme improve the solution accuracy, but at least they do not jeopardize first order accuracy, and neither substantially increase computation time.

Proposition D.5. *Let $u \in \mathbb{U}$ and let $k_*, k^* \geq 0$ be such that $k_* \leq \Lambda u - u \leq k^*$. Then $1 - k^*/\delta_0 \leq u/\boldsymbol{u} \leq 1 + k^*/\delta_0$.*

Proof. Let $s \geq 0$. Then $\Lambda[(1+s)u] \leq (1+s)\Lambda u - \delta_0 s \leq (1+s)(u+k^*) - \delta_0 s$, by δ_0-submultiplicativity. Choosing $s = k^*/(\delta_0 - k^*)$ yields $\Lambda[(1+s)u] \leq (1+s)u$ and thus $(1+s)u \geq \boldsymbol{u}$ by Proposition D.2. On the other hand, $(1+s)\Lambda[u/(1+s)] \geq \Lambda u + s\delta_0 \geq u - k_* + s\delta_0$, again by δ_0-submultiplicativity. Choosing $s = k_*/\delta_0$ yields $\Lambda[u/(1+s)] \geq u/(1+s)$ and thus $u/(1+s) \leq \boldsymbol{u}$ by Proposition D.2. The result follows. □

References

[ABK97] F. Aminzadeh, J. Brac, and T. Kunz. *3-D Salt and Overthrust models*. SEG/EAGE 3-D Modeling Series No.1, 1997.

[AM12] Ken Alton and Ian M Mitchell. An ordered upwind method with precomputed stencil and monotone node acceptance for solving static convex Hamilton-Jacobi equations. *Journal of Scientific Computing*, 51(2):313–348, 2012.

[BC91] Vladislav Babuska and Michel Cara. *Seismic anisotropy in the Earth*, volume 10. Springer Science & Business Media, 1991.

[4] Note that iterative methods, such as fast sweeping, lack the FMM specific concepts of accepted point, post-processing, and frozen value. For this reason, introducing high order finite differences can raise additional challenges, such as numerical instability along iterations.

[BCD08] Martino Bardi and Italo Capuzzo-Dolcetta. *Optimal control and viscosity solutions of Hamilton-Jacobi-Bellman equations*. Springer Science & Business Media, 2008.

[Bey87] G. Beylkin. Mathematical theory for seismic migration and spatial resolution. In M. Bernabini, P. Carrion, G. Jacovitti, F. Rocca, S. Treitel, and M. Worthington, editors, *Deconvolution and inversion.*, pages 291–304. Blackwell scientific publications (Oxford), 1987.

[BL98] F. Billette and G. Lambaré. Velocity macro-model estimation from seismic reflection data by stereotomography. *Geophysical Journal International*, 135(2):671–680, 1998.

[Ble87] N. Bleistein. On the imaging of reflectors in the Earth. *Geophysics*, 52(7):931–942, 1987.

[BLP78] A. Bensoussan, J.L. Lions, and G. Papanicolaou. *Asymptotic analysis of periodic structure*. North-Holland, 1978.

[BLZ10] Jean-David Benamou, Songting Luo, and Hongkai Zhao. A compact upwind second order scheme for the eikonal equation. *Journal of Computational Mathematics*, pages 489–516, 2010.

[BR06] Folkmar Bornemann and Christian Rasch. Finite-element Discretization of Static Hamilton-Jacobi Equations based on a Local Variational Principle. *Computing and Visualization in Science*, 9(2):57–69, June 2006.

[BST83] Iulian Beju, Eugen Soós, and Petre P Teodorescu. *Euclidean tensor calculus with applications*. CRC Press, 1983.

[bW20] Umair bin Waheed. A fast-marching eikonal solver for tilted transversely isotropic mediafast marching anisotropic eikonal solver. *Geophysics*, pages S385–S393, 2020.

[Car01] Michael Carter. *Foundations of mathematical economics*. MIT Press, 2001.

[CBM20] Jian Cao, Romain Brossier, and Ludovic Métivier. 3d acoustic-(visco) elastic coupled formulation and its spectral-element implementation on a cartesian-based hexahedral mesh. In *SEG Technical Program Expanded Abstracts 2020*, pages 2643–2647. Society of Exploration Geophysicists, 2020.

[CC18] Paul Cupillard and Yann Capdeville. Non-periodic homogenization of 3-d elastic media for the seismic wave equation. *Geophysical Journal International*, 213(2):983–1001, 01 2018.

[Cer05] Vlastislav Cerveny. *Seismic ray theory*. Cambridge university press, 2005.

[CM18] Yann Capdeville and Ludovic Métivier. Elastic full waveform inversion based on the homogenization method: theoretical framework and 2-d numerical illustrations. *Geophysical Journal International*, 213(2):1093–1112, 2018.

[CMA+20] P. Cupillard, W. Mulder, P. Anquez, A. Mazuyer, and J. Barthélémy. The apparent anisotropy of the SEG-EAGE overthrust model. In *82th Annual EAGE Meeting*. European Association of Geoscientists & Engineers, 2020.

[Cri09] Emiliano Cristiani. A fast marching method for Hamilton-Jacobi equations modeling monotone front propagations. *Journal of Scientific Computing*, 39(2):189–205, 2009.

[DS97] Joe Dellinger and William Symes. Anisotropic finite-difference traveltimes using a hamilton-jacobi solver. In *SEG Technical Program Expanded Abstracts 1997*, pages 1786–1789. Society of Exploration Geophysicists, 1997.

[FLT03] Masao Fukushima, Zhi-Quan Luo, and Paul Tseng. A sequential quadratically constrained quadratic programming method for differentiable convex minimization. *SIAM Journal on Optimization*, 13(4):1098–1119, 2003.

[GHZ18] Daniel Ganellari, Gundolf Haase, and Gerhard Zumbusch. A massively parallel Eikonal solver on unstructured meshes. *Computing and Visualization in Science*, 19(5-6):3–18, 2018.

[Hes64] HH Hess. Seismic anisotropy of the uppermost mantle under oceans. *Nature*, 203(4945):629–631, 1964.

[JW08] Won-Ki Jeong and Ross T Whitaker. A Fast Iterative Method for Eikonal Equations. *SIAM Journal on Scientific Computing*, 30(5):2512–2534, July 2008.

[KC99] Seongjai Kim and Richard Cook. 3-d traveltime computation using second-order eno scheme. *Geophysics*, 64(6):1867–1876, 1999.

[Kim99] Seongjai Kim. On eikonal solvers for anisotropic traveltimes. In *SEG Technical Program Expanded Abstracts 1999*, pages 1875–1878. Society of Exploration Geophysicists, 1999.

[KS98] R Kimmel and James A. Sethian. Computing geodesic paths on manifolds. *Proceedings of the National Academy of Sciences*, 95(15):8431–8435, July 1998.

[LBBMV17] P Le Bouteiller, M Benjemaa, L Métivier, and J Virieux. An accurate discontinuous Galerkin method for solving point-source Eikonal equation in 2-D heterogeneous anisotropic media. *Geophysical Journal International*, 212(3):1498–1522, 2017.

[LBBMV19] Philippe Le Bouteiller, Mondher Benjemaa, Ludovic Métivier, and Jean Virieux. A discontinuous galerkin fast-sweeping eikonal solver for fast and accurate traveltime computation in 3d tilted anisotropic media. *Geophysics*, 84(2):C107–C118, 2019.

[LCZ14] Haiqiang Lan, Jingyi Chen, and Zhongjie Zhang. A fast sweeping scheme for calculating p wave first-arrival travel times in transversely isotropic media with an irregular surface. *Pure and Applied Geophysics*, 171(9):2199–2208, 2014.

[Lec93] I Lecomte. Finite difference calculation of first traveltimes in anisotropic media. *Geophysical Journal International*, 113(2):318–342, 1993.

[LFH11] Peter G Lelièvre, Colin G Farquharson, and Charles A Hurich. Computing first-arrival seismic traveltimes on unstructured 3-D tetrahedral grids using the fast marching method. *Geophysical Journal International*, 184(2):885–896, 2011.

[LOP+03] G. Lambaré, S. Operto, P. Podvin, Ph. Thierry, and M. Noble. 3-D ray+Born migration/inversion - part 1: theory. *Geophysics*, 68:1348–1356, 2003.

[LQ12] Songting Luo and Jianliang Qian. Fast sweeping methods for factored anisotropic eikonal equations: multiplicative and additive factors. *Journal of Scientific Computing*, 52(2):360–382, 2012.

[LRr13] Wei Liao, Karl Rohr, and Stefan W o rz. Globally Optimal Curvature-Regularized Fast Marching For Vessel Segmentation. *Medical Image Computing and Computer-Assisted Interventation-MICCAI 2013. Springer Berlin Heidelberg.*, pages 550–557, 2013.

[MD17] Jean-Marie Mirebeau and Johann Dreo. Automatic differentiation of non-holonomic fast marching for computing most threatening trajectories under sensors surveillance. In *International Conference on Geometric Science of Information*, pages 791–800. Springer, 2017.

[MD20] Jean-Marie Mirebeau and François Desquilbet. Worst case and average case cardinality of strictly acute stencils for two dimensional anisotropic fast marching. In *Constructive Theory of Functions - 2019*, pages 157–180. Publishing House of Bulgarian Academy of Sciences, 2020.

[Mir14a] Jean-Marie Mirebeau. Anisotropic Fast-Marching on cartesian grids using Lattice Basis Reduction. *SIAM Journal on Numerical Analysis*, 52(4):1573–1599, January 2014.

[Mir14b] Jean-Marie Mirebeau. Efficient fast marching with Finsler metrics. *Numerische Mathematik*, 126(3):515–557, 2014.

[Mir18] Jean-Marie Mirebeau. Fast-marching methods for curvature penalized shortest paths. *Journal of Mathematical Imaging and Vision*, 60(6):784–815, 2018.

[Mir19] Jean-Marie Mirebeau. Riemannian Fast-Marching on Cartesian Grids, Using Voronoi's First Reduction of Quadratic Forms. *SIAM Journal on Numerical Analysis*, 57(6):2608–2655, 2019.

[Mus03] MJP Musgrave. *Crystal acoustics*. Acoustical Society of America New York, 2003.

[MvN92] T. J. Moser, T. van Eck, and G. Nolet. Hypocenter determination in strongly heterogeneous earth models using the shortest path method. *Journal Geophysical Research*, 97:6563–6572, 1992.

[Nol08] G. Nolet. *A Breviary of Seismic Tomography*. Cambridge University Press, Cambridge, UK, 2008.

[OS91] Stanley Osher and Chi-Wang Shu. High-order essentially nonoscillatory schemes for hamilton–jacobi equations. *SIAM Journal on numerical analysis*, 28(4):907–922, 1991.

[PWZ17] Amit Padhi, Mark Willis, and Xiaomin Zhao. Accurate quasi-p traveltimes in 3d transversely isotropic media using a high-order fast-sweeping-based eikonal solver. In *SEG Technical Program Expanded Abstracts 2017*, pages 369–373. Society of Exploration Geophysicists, 2017.

[QZZ07] Jianliang Qian, Yong-Tao Zhang, and Hong-Kai Zhao. A fast sweeping method for static convex hamilton–jacobi equations. *Journal of Scientific Computing*, 31(1-2):237–271, 2007.

[RS04] Nick Rawlinson and Malcolm Sambridge. Multiple reflection and transmission phases in complex layered media using a multistage fast marching method. *Geophysics*, 69(5):1338–1350, 2004.

[RS07] Christian Rasch and Thomas Satzger. Remarks on the O(N) Implementation of the Fast Marching Method. *arXiv.org*, March 2007.

[Set96] James A. Sethian. A fast marching level set method for monotonically advancing fronts. *Proceedings of the National Academy of Sciences*, 93(4):1591–1595, 1996.

[Set99] James A. Sethian. *Level Set Methods and Fast Marching Methods: Evolving Interfaces in Computational Geometry, Fluid Mechanics, Computer Vision, and Materials Science*. Cambridge University Press, 1999.

[Sla03] Michael A Slawinski. *Seismic waves and rays in elastic media*, volume 34. Elsevier, 2003.

[SV01] James A. Sethian and Alexander Boris Vladimirsky. Ordered upwind methods for static Hamilton-Jacobi equations. *Proceedings of the National Academy of Sciences of the United States of America*, 98(20):11069–11074 (electronic), 2001.

[TBM+19] Phuong Thu Trinh, Romain Brossier, Ludovic Métivier, Laure Tavard, and Jean Virieux. Efficient 3D time-domain elastic and viscoelastic Full Waveform Inversion using a spectral-element method on flexible Cartesian-based mesh. *Geophysics*, 84(1):R75–R97, 2019.

[TCO04] YHR Tsai, LT Cheng, and S Osher. Fast sweeping algorithms for a class of Hamilton-Jacobi equations. *SIAM Journal on Numerical Analysis*, 2004.

[TCOZ03] Yen-Hsi Richard Tsai, Li-Tien Cheng, Stanley Osher, and Hong-Kai Zhao. Fast sweeping algorithms for a class of hamilton–jacobi equations. *SIAM journal on numerical analysis*, 41(2):673–694, 2003.

[TH16] Eran Treister and Eldad Haber. A fast marching algorithm for the factored eikonal equation. *Journal of Computational Physics*, 324:210–225, 2016.

[Tho86] Leon Thomsen. Weak elastic anisotropy. *Geophysics*, 51(10):1954–1966, 1986.

[TNCC09] C. Taillandier, M. Noble, H. Chauris, and H. Calandra. First-arrival travel time tomography based on the adjoint state method. *Geophysics*, 74(6):WCB1–WCB10, 2009.

[Tsi95] J.N. Tsitsiklis. Efficient algorithms for globally optimal trajectories. *IEEE transactions on Automatic Control*, 40(9):1528–1538, September 1995.

[Vid88] John Vidale. Finite-difference calculation of travel times. *Bulletin of the Seismological Society of America*, 78(6):2062–2076, 1988.

[VN18] Donald W Vasco and Kurt Nihei. Broad-band trajectory mechanics. *Geophysical Journal International*, 216(2):745–759, 2018.

[WYF15] Umair Bin Waheed, Can Evren Yarman, and Garret Flagg. An iterative, fast-sweeping-based eikonal solver for 3d tilted anisotropic media. *Geophysics*, 80(3):C49–C58, 2015.

[Zha05] Hongkai Zhao. A fast sweeping method for eikonal equations. *Mathematics of computation*, 74(250):603–627, 2005.